

**CFD Comparative Study of 3-D Compressible Flow Over Seamless  
and Canard Aerodynamic Flying Bodies**

by

Tan Han Boon

16483

Dissertation submitted in partial fulfilment of  
the requirements for the  
Bachelor of Engineering (Hons)  
(Mechanical Engineering)

JANUARY 2016

Universiti Teknologi PETRONAS  
Bandar Seri Iskandar  
31750 Tronoh  
Perak Darul Ridzuan

## **CERTIFICATION OF APPROVAL**

### **CFD Comparative Study of 3-D Compressible Flow Over Seamless and Canard Flying Bodies**

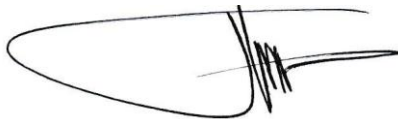
by

Tan Han Boon

16483

A project dissertation submitted to the  
Mechanical Engineering Programme  
Universiti Teknologi PETRONAS  
in partial fulfillment of the requirement for the  
BACHELOR OF ENGINEERING (Hons)  
(MECHANICAL ENGINEERING)

Approved by,



---

JUNDIKA CANDRA KURNIA

UNIVERSITI TEKNOLOGI PETRONAS

TRONOH, PERAK

January 2016

## **CERTIFICATION OF ORIGINALITY**

This is to certify that I am responsible for the work submitted in this project, that the original work is my own except as specified in the references and acknowledgements, and that the original work contained herein have not been undertaken or done by unspecified sources or persons.



---

TAN HAN BOON

## ABSTRACT

Today, many aerodynamic flying bodies have installed canard to enhance its maneuverability. However, up to this date, there is no direct comparison of flow field and aerodynamic characteristics that have been made between a seamless and canard. The impact of the canard on the aerodynamic characteristics of a flying body is also not clearly defined. Hence, this project is designed to conduct a series of investigation to compare the influence of canard to the aerodynamic flow field and characteristics as compared to a seamless flying body.

To achieve the objectives, Computational Fluid Dynamic (CFD) and DATCOM simulations are conducted to evaluate the flow field and the aerodynamic forces and moment coefficients of the flying bodies at Mach 2.0 and at 5 different angles of attack (AOA) up to  $10^\circ$ . The flying bodies are assumed to be operating at 1500 meter from sea level. The software used is ANSYS FLUENT and USAF Digital DATCOM. Two equations, standard  $k-\varepsilon$  turbulent model is used to analyze turbulent viscous effect in the flow field. The evaluated aerodynamic coefficients are axial force ( $C_A$ ), normal force ( $C_N$ ), drag, ( $C_D$ ), lift ( $C_L$ ) and pitching moment ( $C_M$ ).

The simulation results show CFD and DATCOM have a relatively good agreement in  $C_A$  and  $C_D$  while DATCOM over-predicts the value for  $C_L$ ,  $C_M$  and  $C_N$ . As an additional pressure difference develops and forms extra force component at the canard, the canard body yields higher aerodynamic coefficients than seamless body in overall. Besides that, contour plot presents the formation of shock wave at the nose, canard and tail-fin and wake at the rear region of the main body, which resembles the typical flow field of a high Reynolds Number flow. Shock wave and wake angle are observed to have changed when an AOA is applied. The AOA also promotes the formation of vortices above the main body, canard and tail-fin. In addition, the flow downwash from the canard accumulates a higher temperature at the wing root of its tail-fin. The vortices at the canard also propagate downstream as an effect of downwash, thereby increasing the vorticity intensity at the tail-fin region.

## **ACKNOWLEDGEMENT**

I would like to express my utmost gratitude to my advisors, Dr. Jundika Candra Kurnia and Professor Dr. Hussain Al-Kayiem for their continuous support of this dissertation research. This dissertation became possible due to their guidance, wisdom and motivation throughout the research activities. Thank you to Dr Jundika Candra Kurnia for teaching me extensive knowledge on the application of Computational Fluid Dynamics and its related post-processing procedure in solving aerodynamic problems. My sincere gratitude goes to Professor Dr Hussain Al-Kayiem for nurturing a passion towards supersonic, compressible flow that allowed me to execute this research with full enthusiasm.

I thank the Department of Mechanical Engineering of Universiti Teknologi PETRONAS for supporting this research by providing the necessary IT tools and analysis software, such as SolidWorks and ANSYS FLUENT.

Last but not least, I would like to thank my family and friends for giving me support spiritually throughout the dissertation writing and my academic endeavor.

## TABLE OF CONTENTS

CERTIFICATION OF APPROVAL .....	ii
CERTIFICATION OF ORIGINALITY .....	iii
ABSTRACT.....	iv
ACKNOWLEDGEMENT .....	v
LIST OF FIGURES .....	viii
LIST OF TABLES .....	x
ABBREVIATION AND NOMENCLATURE.....	xi
CHAPTER 1: INTRODUCTION .....	1
1.1 BACKGROUND.....	1
1.2 PROBLEM STATEMENT .....	2
1.3 OBJECTIVES .....	2
1.4 SCOPE OF STUDY .....	2
CHAPTER 2: LITERATURE REVIEW .....	5
2.1 MATHEMATICAL MODELING OF SUPERSONIC FLOW ....	5
2.2 SIMULATION APPROACHES IN SUPERSONIC FLOW .....	7
2.3 AERODYNAMIC CHARACTERISTIC OF FLYING BODY ....	8
CHAPTER 3: METHODOLOGY .....	16
3.1 CALCULATION.....	16
3.1.1 Operating Temperature and Pressure .....	16
3.1.2 Free Stream Velocity and Reynolds Number .....	16
3.2 CFD SIMULATION .....	17
3.2.1 Governing Equations .....	17
3.2.2 Geometry Modeling.....	19

3.2.3	Computational Grid Generation for Seamless and Canard Body.....	20
3.2.4	CFD Flow Model Formulation .....	22
3.2.5	CFD Results Validation.....	23
3.3	SEMI-EMPIRICAL SIMULATION.....	24
3.3.1	Computation in USAF Digital DATCOM.....	24
3.3.2	Result Post-Processing in MATLAB .....	25
3.4	PROJECT MANAGEMENT APPROACH.....	25
CHAPTER 4:	RESULTS .....	28
4.1	CFD RESULTS AND INTERPRETATION .....	28
4.1.1	Slender Body .....	28
4.1.2	Seamless and Canard Flying Body .....	30
CHAPTER 5:	CONCLUSION AND RECOMMENDATION .....	48
5.1	CONCLUSION .....	48
5.2	RECOMMENDATION.....	48
REFERENCES.....		50
APPENDICES A.....		53

## LIST OF FIGURES

FIGURE 1: Lift ( $L$ ), Drag ( $D$ ), Normal ( $N$ ) and Axial ( $A$ ) Forces and Pitching Moment ( $M$ ) on Center of Pressure ( $C.P$ ). .....	1
FIGURE 2: Geometries and Dimensions of (a) Seamless and (b) Canard Flying Body. ....	3
FIGURE 3: The Behaviour of Lift ( $C_L$ ), Drag ( $C_D$ ) and Pitching Moment ( $C_M$ ) Coefficient at Different AOA Values [9]. ....	9
FIGURE 4: Seamless (Left) and Canard (Right) Body Geometry in SolidWorks. .	19
FIGURE 5: Seamless Body Enclosed in Flow Domain. ....	20
FIGURE 6: Overall Mesh of the Flow Domain for the Flying Body. ....	21
FIGURE 7: Close Up Mesh of the Seamless Body. ....	21
FIGURE 8: Close Up Mesh of the Canard Body. ....	21
FIGURE 9: Flow Domain, Labeled With Named Surfaces. ....	22
FIGURE 10: Process Flow of CFD and DATCOM Simulation. ....	25
FIGURE 11: Project's Key Milestone. ....	26
FIGURE 12: (Above) Dimensions of the Slender Body, (Bottom) Mesh of the Slender Body. ....	28
FIGURE 13: (From Top Left to Bottom Left, Clockwise) Contour of Static Pressure, Density, Velocity and Static Temperature for Slender Body. ....	29
FIGURE 14: Theoretical Shock Wave Angle of Slender Body as Indicated in $\theta_c$ - $\theta_s$ - $M$ Diagram [1]. ....	30
FIGURE 15: $C_D$ variation vs Number of Element of Seamless and Canard Body....	31
FIGURE 16: Aerodynamic Coefficients of Seamless (Left) and Canard (Right) versus Angle of Attack. ....	33
FIGURE 17: Lift to Drag Coefficient Ratio of Seamless and Canard Body .....	35
FIGURE 18: Pressure Contour Showing the Shock Wave of Seamless (Left) and Canard (Right) at (a) AOA $0^\circ$ , (b) AOA $2.5^\circ$ , (c) AOA $5.0^\circ$ , (d) AOA $7.5^\circ$ and (e) AOA $10.0^\circ$ .....	36



FIGURE 19: Temperature Contour Showing the Shock Wave of Seamless (Left) and Canard (Right) at (a) AOA 0°, (b) AOA 2.5°, (c) AOA 5.0°, (d) AOA 7.5° and (e) AOA 10.0° .....	37
FIGURE 20: Density Contour Showing the Shock Wave of Seamless (Left) and Canard (Right) at (a) AOA 0°, (b) AOA 2.5°, (c) AOA 5.0°, (d) AOA 7.5° and (e) AOA 10.0° .....	38
FIGURE 21: Velocity Contour Showing the Shock Wave of Seamless (Left) and Canard (Right) at (a) AOA 0°, (b) AOA 2.5°, (c) AOA 5.0°, (d) AOA 7.5° and (e) AOA 10.0° .....	39
FIGURE 22: Pressure Contour at AOA = 10° of (a) Seamless and (b) Canard Body at $x = 0.5$ m, 5.5 m and 8.5 m. ....	41
FIGURE 23: Pressure Distribution on the Seamless (Top Row) and Canard (Bottom Row) Body.....	42
FIGURE 24: Temperature Distribution on Seamless (Top Row) and Canard (Bottom Row) Body.....	43
FIGURE 25: Flow Recirculation at Wake Region (Cyan-Blue Color Region) of Seamless Body.....	44
FIGURE 26: Vortices Formation of (Left) Seamless and (Right) Canard Body at $x = 5.5$ m at Multiple AOAs. ....	45
FIGURE 27: Vortices Formation of (Left) Seamless and (Right) Canard Body at $x = 8.5$ m at Multiple AOAs. ....	46
FIGURE 28: Scaled Residual for CFD Simulation of Seamless Body at Mach 2.0 and AOA 0° . ....	57
FIGURE 29: $C_D$ Plot against Iterations of Seamless Body.....	57
FIGURE 30: DATCOM Simulation Results in MATLAB for Seamless Body. ....	60
FIGURE 31: DATCOM Simulation Results in MATLAB for Canard Body.....	60

## LIST OF TABLES

TABLE 1: Comparison of Relevant CFD Findings from Various Authors. ....	12
TABLE 2: Boundary Conditions and Parameters of the Solver. ....	23
TABLE 3: Gantt Chart and Key Milestones. ....	27
TABLE 4: Aerodynamic Coefficients for Seamless Body, CFD. ....	32
TABLE 5: Aerodynamic Coefficients for Canard Body, CFD. ....	32
TABLE 6: Aerodynamic Coefficients for Seamless Body, DATCOM. ....	32
TABLE 7: Aerodynamic Coefficients for Canard Body, DATCOM. ....	32
TABLE 8: Mesh Independency Study Results for Slender Body. ....	53
TABLE 9: Mesh Independency Study for Seamless Body, PART 1. ....	54
TABLE 10: Mesh Independency Study for Seamless Body, PART 2. ....	54
TABLE 11: Finalized Mesh Parameters for Seamless Body. ....	55
TABLE 12: Mesh Independency Study for Canard Body, PART 1. ....	55
TABLE 13: Mesh Independency Study for Canard Body, PART 2. ....	56
TABLE 14: Finalized Mesh Parameters for Canard Body. ....	56
TABLE 15: Boundary Conditions for the Named Selection Surface Inlet, Outlet and Far Field. ....	57

## ABBREVIATION AND NOMENCLATURE

AOA, $\alpha$	Angle of Attack
CFD	Computational Fluid Dynamic
$C_A$	Axial Force Coefficient
$C_D$	Drag Force Coefficient
$C_L$	Lift Force Coefficient
$C_M$	Pitching Moment Coefficient
$C_N$	Normal Force Coefficient
$C.P$	Center of Pressure
$A$	Axial Force
$D$	Drag Force
$L$	Lift Force
$M$	Pitching Moment
$N$	Normal Force
$\theta_c$	Nose Cone Angle
$\theta_s$	Shock Wave Angle
$\gamma$	Specific Heat Ratio
$V'$	Nondimensional Velocity in Shock Wave
$V'_r$	Radial Velocity in Shock Wave
$V'_\theta$	Polar Velocity in Shock Wave
RANS	Reynolds-Average Navier-Stokes
$k$	Turbulent Kinetic Energy
$\varepsilon$	Turbulent Dissipation
$\rho$	Air Density
$\nu_T$	Kinematic Turbulent Viscosity
$C_\mu$	Model Constant
$\mu_t$	Eddy Viscosity
$\tau_{ij}$	Reynolds Stress Tensor
$S_{ij}$	Mean Strain Rate
$\delta_{ij}$	Kronecker delta
$C_\mu, C_{\varepsilon 1}, C_{\varepsilon 2}, \sigma_k, \sigma_\varepsilon$	Turbulence Model Constant

# CHAPTER 1

## INTRODUCTION

### 1.1 BACKGROUND

The understanding of aerodynamic characteristics of the flow field over seamless and canard aerodynamic flying body, such as rocket and missile is crucial to determine the effects of the canard on the flying body's maneuverability. With an increased agility of flying body in military and aerospace application, it can experience up to supersonic flow and high angle of attack (AOA) in its post-launch trajectories. The interaction between air and the flying body during its trajectory will yield aerodynamic forces and moments. Figure 1 shows the aerodynamic forces including lift ( $L$ ), drag ( $D$ ), normal ( $N$ ) and axial ( $A$ ). Meanwhile, pitching moment will also form about the center of pressure ( $C.P$ ). These forces are commonly defined in terms of coefficient, such as axial force ( $C_A$ ), normal force ( $C_N$ ), drag, ( $C_D$ ), lift ( $C_L$ ), pitching moment ( $C_M$ ) and center of pressure ( $C.P$ ) coefficients. The sources of these forces are mainly pressure and shear stress distribution over the body surface [1].

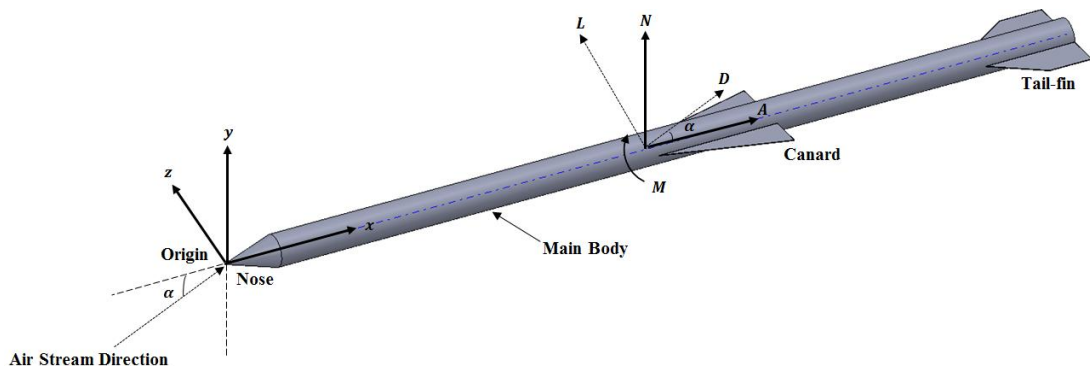


FIGURE 1: Lift ( $L$ ), Drag ( $D$ ), Normal ( $N$ ) and Axial ( $A$ ) Forces and Pitching Moment ( $M$ ) on Center of Pressure ( $C.P$ ).

On the other hand, shock waves will also form at the leading edges of the body and wings at supersonic speed. The shock waves are a thin region, across which the flow properties such as pressure, density and temperature will change drastically [1-3].

The prediction of aerodynamic loads is important in stability and control assessment while the aerothermal characteristics are used to select insulating surface material against aerodynamic heating [4]. Typically, the flow field can be evaluated in various approaches, which are numerically and experimentally. In this project, the main simulation approach is the Computational Fluid Dynamic (CFD) technique.

## **1.2 PROBLEM STATEMENT**

The addition of canard onto a flying body will not only affect its flow field parameters, but also its resultant aerodynamic forces and moments.

In a supersonic and turbulent flow, shock waves, vortices and wakes could form at the canard's surrounding and these will change the properties of the flow field at its subsequent areas such as density, pressure and temperature distribution on its tail fins. Furthermore, the canard configuration could have better maneuverability as compared to a seamless body. However, the additional surface area projected by the canard would possibly change the aerodynamic characteristics on the body.

## **1.3 OBJECTIVES**

This project aims to quantitatively predicts and compares the aerodynamic characteristics, including the forces and moment coefficients, between seamless and canard flying body.

Besides that, this project also investigate the effect of canard on the compressible flow field structure around a supersonic flying body, which includes the shock waves and vortices behavior as well as density, pressure, temperature and velocity distribution..

## **1.4 SCOPE OF STUDY**

This study focuses on the comparison of flow field across two different geometries of aerodynamic flying bodies, namely seamless and canard configuration. Same as the tail-fin, the canard is assumed to be a fixed forewing with zero deflection. The primary simulation approach is CFD technique using ANSYS FLUENT solver. The altitude is assumed to be at 1,500 meter above sea level. Figure 2 shows the seamless and canard body's geometries which will be simulated.

Based on Figure 2, a seamless body has a pair of tail fins while its remaining length is in cylindrical. Meanwhile, a canard body has an additional pair of canards (forewings) ahead of its tail-fins. In the present research, the tail-fins are assumed to be trapezoidal shape with a fin span of 966 mm and a thickness of 5 mm. For canard body, the canards are in delta shape with a same span as its tail-fins. The total length for both bodies is 8500 mm. The nose of both bodies is in conical shape.

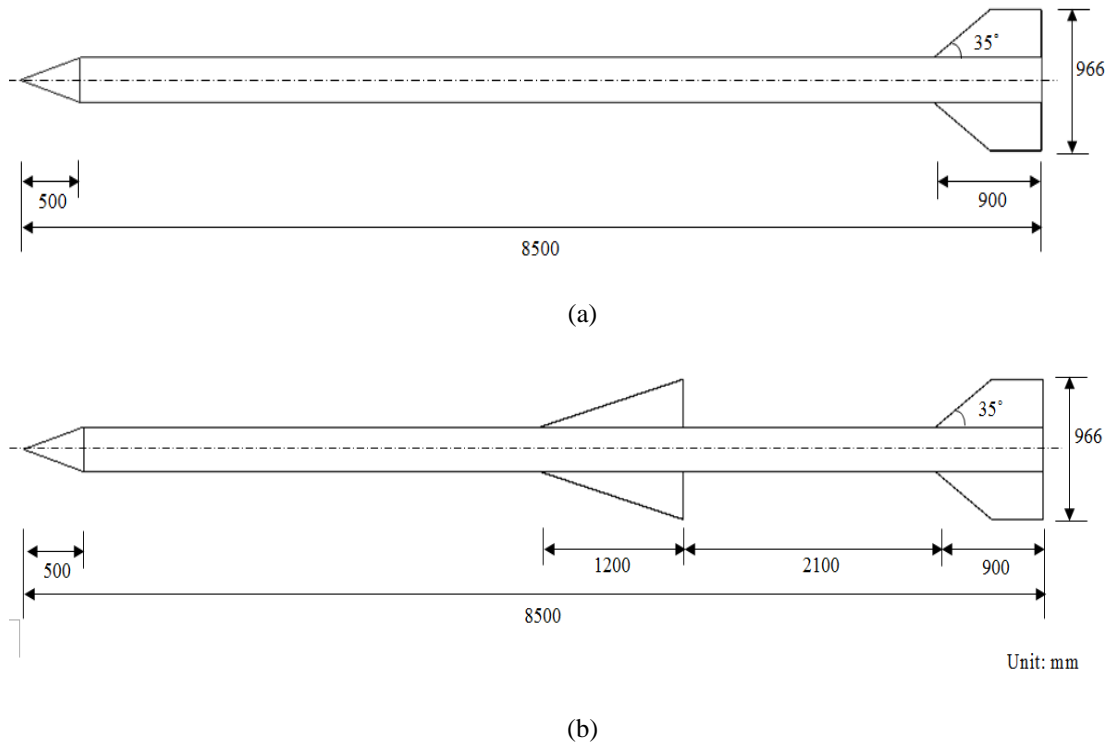


FIGURE 2: Geometries and Dimensions of (a) Seamless and (b) Canard Flying Body.

The seamless and canard body designs are widely implemented in space and military industry and they are propelled with high thrust to achieve a very high speed for fast-moving object's targeting. Hence, the flow speed being studied here is focused on supersonic speed at Mach 2.0. To simulate the modern projectile with robust agility and high turn rates, five different AOAs, namely  $0^\circ$ ,  $2.5^\circ$ ,  $5^\circ$ ,  $7.5^\circ$  and  $10^\circ$  will be simulated for each design. Thus, a total of 10 CFD simulations will be conducted.

The CFD results will be validated using the Taylor-Maccoll Equation by evaluating its shock wave behavior. A semi-empirical simulation will also be conducted using USAF Stability and Control (USAF) Digital DATCOM and its results will be compared to the CFD results obtained from ANSYS FLUENT. Same as CFD simulation, a total of ten semi-empirical simulations will be conducted to investigate

if both results achieve a good agreement. The aerodynamic characteristics will then be identified for both seamless and canard body. The detailed procedure of modeling and setting up the simulation will be explained in Chapter 3: Methodology.

All the required IT tools and software, such as ANSYS FLUENT and MATLAB are readily available in the Computer Aided Engineering Laboratory in Universiti Teknologi PETRONAS. The computers in the laboratory are in up-to-date status with good computational power, hence a converged solution from the CFD simulations can be obtained in a shorter computational time. Therefore, the feasibility of this study in terms of cost and time is justified.

The findings from this study are expected to serve as a guideline in the design process of a flying body with a consideration of canard installation in order to accomplish the desired flying performance. The impacts of the canard on both flow field and aerodynamic forces coefficients are strongly emphasized in this study. Depending on the application, the aerodynamicists can refer to these findings and justify if the canard is necessary in designing of the flying body. It also contributes to a better understanding on the aerodynamic characteristics of canard configuration which enables the aerospace and mechanical engineers to optimize the design of the flying body in achieving the essential maneuverability, fuel efficiency and stability control. This study also reveals the pressure and temperature distributions on a projectile-shape flying body, thus allowing structural and material engineers to determine the potential locations with high pressure and accumulated aerodynamic heating. From there, the structure at the particular location can be strengthened and an appropriate material could be adopted.

## CHAPTER 2

### LITERATURE REVIEW

#### 2.1 MATHEMATICAL MODELING OF SUPERSONIC FLOW

The governing equation for a fluid flow is dependent on the flow type and model being assumed. For example, a viscous flow which includes transport phenomena of friction, thermal conductivity and mass diffusion is governed by Navier-Stokes Equations and it consists of Continuity, Momentum and Energy Equation [5].

If the viscous effect is neglected, the governing equation will be different as the viscous terms in the equations will be neglected. In [6], Al-Kayiem et al. modeled the supersonic flow field over a seamless missile as frictionless. In this case, the flow was governed by Euler Equations, a variation of Navier-Stokes with all the viscous terms being neglected. Considering the pressure force will overwhelm the viscous effect at supersonic speed, the inviscid, compressible flow model is suitable in their study and capable of providing a result with reasonable accuracy [5]. Euler Equations was also used in [7] to predict the aerodynamic coefficients and stability derivatives of a civil canard airplane, Firefly developed by Korea Aerospace Research Institute.

In contrast, some of the researchers took the viscous effect into consideration while studying the flow field over a flying body of complex geometry. In [8], [9], [10], [11], [12], [13], [14], [15], [16], [17] and [18], the flow was modeled as viscous and compressible. In their cases, the flow was governed by Reynolds-Averaged Navier-Stokes (RANS) Equations, a modified version of Navier-Stokes Equation, which an additional unknown term called Reynolds Stress is introduced [11]. Since the flow was of high Reynolds Number, turbulence viscous effect was adopted in their studies. Ridluan [11], Sahu et al. [12], Gulay et al. [14], Zhang et al. [15], Kaleeswaran et al. [17] and Cummings et al. [19] have modeled the viscous effect in their researches with standard  $k$ - $\varepsilon$  turbulent model where the turbulence viscosity was computed in terms of turbulent kinetic energy,  $k$  and turbulent dissipation,  $\varepsilon$ . Besides that, Zhang



et al. [9], Li et al. [13], Xie et al. [16], Anand et al. [18] and Sinde et al. [20] used Spalart-Allmaras (S-A) model which solved for an unknown viscosity-like term,  $\tilde{\nu}$  called Spalart-Allmaras variable. S-A model is specialized in the prediction of boundary layer involving pressure gradient [21]. On the other hand, Shear Stress Transport (SST)  $k-\omega$  model was used by Wee [8], Tomi et al. [10] and Sohail et al. [22] to solve  $k$  and specific dissipation,  $\omega$  which represents the scale of flow turbulence. In fact, there are also other variations of  $k-\omega$  model such as Menter's SST  $k-\omega$  model etc. The effect of  $k-\omega$  model variations was investigated by Kwak et al. and their results revealed that the effect of  $k-\omega$  model variations on aerodynamic coefficients is insignificant [23]. In [14], the flow over a wrap-around-finned (WAF) missile was simulated with three different turbulent models to investigate the effect of viscous models on the results. Similarly, Akgul et al. [24] evaluated the supersonic flow over a canard missile using 3 turbulent models, including  $k-\varepsilon$ , S-A and  $k-\omega$  model. They justified that  $k-\varepsilon$  model is more suitable in such analysis due to a relatively more accurate pitching moment value prediction as well as a faster solution converging time than the  $k-\omega$  model. Similarly, Cummings et al. [19] revealed that  $k-\varepsilon$  model can predict the viscous features of a flow adequately, which include shock wave, expansion fans and flow recirculating region. Sohail et al. [22] also compared the performance of Euler method and SST  $k-\omega$  turbulent model in supersonic flow over seamless body. They justified that Euler method slightly under-predicted the aerodynamic coefficients, as the viscous effect is neglected, while the  $k-\omega$  model achieved high agreement with the experimental results. In overall, despite the variation of viscous models being used, their simulation results displayed good agreement with experimental or semi-empirical data obtained from previous researches. It is further elaborated in the next section, 3.2 CFD Simulation.

Moreover, Partial Averaged Navier-Stokes (PANS) has also been used by Luo et al. [25] to analyze supersonic turbulent-separated flows over ramped-cavity flight vehicle. Here, a new term,  $f_k$  is introduced and it can be assumed either a variable (for  $k-\omega$  based model) or a constant (for  $k-\varepsilon$  based model). From his result, he revealed that variable  $f_k$  produced a higher agreement to the RANS approach, while constant  $f_k$  produced a poorer agreement result.

Large Eddy Simulation (LES) has been used by Dal et al. [26] to simulate the flow field of high Reynolds Number around a cylindrical afterbody. In his research, he proved that LES could potential predict the turbulent properties and formation of large eddies in the flow downstream more accurate as compared to RANS approach.

## **2.2 SIMULATION APPROACHES IN SUPERSONIC FLOW**

In Section 2.1 Background Study, it is mentioned that the flow over an object can be simulated numerically or experimentally and they are implemented used today.

CFD approach was implemented in [6], [8], [9], [10], [11], [12], [13], [14], [15], [16], [17] [18], [25] and [26] to solve the governing equations for flow simulation. Al-Kayiem et al. [6] have implemented an in-house computer code which solved a set of finite difference discretized Euler Equation using Time-Marching MacCormack's explicit technique at a Mach Number of 1.5 over a seamless missile. Other than that, Wee [8], Zhang et al. [9], Honkanen et al. [10], Ridluan [11], Sahu et al [12], Li et al. [13], Gulay et al. [14] and Xie et al. [16] have used commercial CFD solver to solve RANS Equations with turbulent viscosity. Most of them used ANSYS FLUENT solver, except in [8], [10] and [12] which used ANSYS CFX, OpenFOAM and CFD++ solver respectively. All those solvers are capable to generate an accurate result and visualize the flow field, provided the physics and boundary conditions are being applied in a proper way.

Some of them also extended their researches to semi-empirical simulation and wind tunnel testing. Missile DATCOM, a computer program which evaluates aerodynamic characteristics of a missile semi-empirically, was used in [9] and [11] to validate their CFD results. According to Blake and Gillard [27], Missile DATCOM has built in vortex model to consider vortex interference effects, therefore it is capable to predict the aerodynamic coefficients with good accuracy at low AOA. However, the prediction accuracy starts to degrade when it reach moderate or higher AOA, specifically beyond  $10^\circ$ . Similarly, other semi-empirical tool like Aeroprediction 09 (AP09) was used in [8] for the same purpose. Dahalan et al. has developed a computer program based on USAF Digital DATCOM algorithm to estimate the aerodynamic coefficient of a rocket semi-empirically and it is capable of producing simulation results of good agreement with the experimental results [28]. However, in

many cases the DATCOM software inaccurately predicted the value for  $C_N$  of projectile-shape geometry [7, 11, 29]. Over-prediction of  $C_M$  of canard body has also been reported by Akgul et al. [24]. Hence, Maurice [29] and Abney and McDaniel [30] proposed that an error correction factor should be derived to correct the value closer to the CFD and experimental results. These correction factors should also be specific for each geometry and there is no correction factor that is generally applicable for all geometries. In overall, DATCOM still serves as a great comparison tool for  $C_A$  value. Other prediction codes such as MISL3 and MISDL have been used by Lesieutre and Quijano [31] and the prediction results could achieve good agreement with experimental results. Celiker et al. [32] suggested that for preliminary analysis, the semi-empirical approach can be adopted but more sophisticated approach such as CFD should be used in detailed design studies which require high accuracy. Likewise, some researchers validated the CFD results with wind tunnel test data for higher accuracy results closer to realistic flow. Zhang et al. [9] has conducted experimental simulation on its Theater Ballistic Missile Target (TBMT) model using a supersonic wind tunnel. By using Schlieren photo, the oblique shock waves over the TMBT model were visualized. Leopold et al. [33] visualized the flow field features, such as shock wave and vortices by using a laser Doppler velocimeter (LDV). Meanwhile, Li et al. [13] also demonstrated the usage of low speed wind tunnel, with its resulting data corrected with Karman-Tsien Rule, to experimentally predict the aerodynamic characteristics at higher subsonic speed and the results displayed good agreement with CFD results.

### **2.3 AERODYNAMIC CHARACTERISTIC OF FLYING BODY**

Most aerodynamicists are concern about the aerodynamic coefficients, such as  $C_L$ ,  $C_D$ ,  $C_A$ ,  $C_N$  and  $C_M$ . The analysis of aerodynamic coefficients of rockets, missiles and projectiles are documented in [8], [9], [10], [11], [12], [13], [15] and many more on the similar geometries. Center of pressure,  $C.P$  location was also analyzed by Zhang et al. [3] in the study on flow field over TMBT.

These aerodynamic characteristics are dependent on the body's geometry, Mach Number, AOA and so on. Ridluan [11] has studied the effects of Mach Number and AOA on the aerodynamic coefficients on a seamless missile. His study revealed the aerodynamic coefficients at constant positive AOA reach maximum within transonic

flow, particularly at Mach 1. On the other hand, upon the increment of AOA,  $C_D$ ,  $C_L$  and  $C_M$  will increase when the Mach Number is remained constant. A similar behavior is also discovered on the simulated flow field over a canard flying body in [8], [9] and [13]. Figure 3 shows the behavior of  $C_L$ ,  $C_D$  and  $C_M$  over various AOA, studied by Zhang et al.

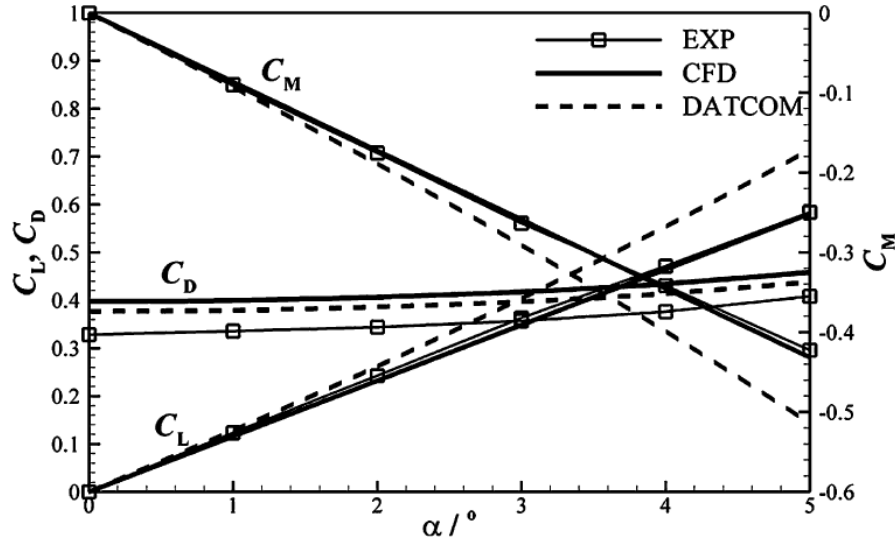


FIGURE 3: The Behaviour of Lift ( $C_L$ ), Drag ( $C_D$ ) and Pitching Moment ( $C_M$ ) Coefficient at Different AOA Values [9].

Beyond that, Tomi et al. [10] studied the flow field over a split-canard missile in turbulent subsonic flow. His study emphasized on the comparison between the effect of split-canard and single-canard to the  $C_M$  and  $C_N$ , which appear to be distinctive at high AOA. His results revealed that the lift produced by the tail fin overwhelmed the aerodynamic effect of the single-canard configuration much easier as compared to the split-canard configuration. Here, it displayed the enhancement of maneuverability by the split-canard as compared to single-canard. Furthermore, the relative position of canard from tail fin and features of canard vortices were also discovered as one of the factor that affects aerodynamic characteristics [15].

The simulated aerodynamic characteristics can also be visualized in contour and vector form. In [11], Ridluan used the combination of both contour and vector to evaluate the behavior of shock waves and vortices formation on a seamless missile. His results showed the formation of shock waves at the warhead and before the tail fins at supersonic speed. Besides that, vortices formation is detected particularly at the missile's upper surface, when the AOA is positive. Meanwhile, the vortices could

also disappear due to pressure shock pattern, specifically when the shock waves meet at that particular area. Other than using contour or vector approach, shock waves can also be detected using mathematical approach. This mathematical approach is adopted by Kanamori and Suzuki [34], which the approach detects the convergence of flow characteristics and calculates the eigenvectors for the propagation velocity of the Riemann invariants. It can be used as a useful detection method to understand the complex flow structure associated with the shock waves formation.

Meanwhile, Anand et al. simulated the flow field over a canard-wing configuration flying body and discovered that vortices will form at the downstream of canard [18]. These vortices interact with the main wing and the flow field properties at the region will be altered, depending on the distance of canard from the main wing. Vortices formation on canard surface was also investigated in [16]. At small AOA, the canard vortices may also affect the static pressure distribution on the tail fins' leading edge. This effect starts to diminish when the AOA increases as the canard vortices have a lesser tendency to reach the tail fins. According to Akgul et al. [35], the presence of canard could decrease the normal force component on the main wing in supersonic flow. However, such effect is independent of the size and position of the canard.

The effect of canard is further investigated by Nasir et al. on a blended wing flying body using the wind tunnel experimental approach [36]. Their results revealed that  $L/D$  ratio of the flying body may be reduced. They interpreted that the  $L/D$  can be improved by changing the main wing location forward even more instead of having it at the very rear part of the flying body. Zurriati et al. [37] also conducted similar experiment and justified that the canard has high influence on the pitching moment coefficient,  $C_M$  of the blended wing flying body while the canard setting angle does not significantly affect the lift coefficient. In parallel, Lopes et al. [38] emphasized the importance of canard design and location relative to the tail-fin as the canard will contribute additional lift force which could be undesired for some applications.

Simulation and experiment were also conducted by Shi et al. [39] to investigate asymmetric vortex behavior over a seamless body with chinned fuselage and trapezoidal swept wing. Their findings revealed that fuselage vortical flow possesses significant effect on its tail-fin vortices behavior. The vortices from the fuselage can delay the breakdown of wing vortices and this effect is weakened upon the increment

of AOA. A similar finding is also made by Samimi et al. [40] where the presence canard postpones the vortex formation on the tail-fin at subsonic flow.

Nevertheless, the influence of wing-tip shape on the vortices behavior had been experimentally investigated by Giuni and Green [41] between squared and rounded wing-tip. Squared wing-tip was discovered to have produced various primary vortex structures accompanied by secondary vortex. Both primary and second vortex interacts with each other and induced instability within the primary vortex, subsequently contributes to meandering effect. The vortices behavior produced at the rounded wing-tip is relatively steady with a less intense secondary vortex. Their work also demonstrated the importance of vortices analysis at different geometries in controlling vortices during wing design. Based on the findings by Davari et al. [42], the vortices formation from the main wing or canard is not only affected by wing design, but also the wing-to-tail span ratio and nose-body vortices interference. Among these factors, they justified that the main wing's aspect ratio contributes the dominant effect on the flow field structure at the tail-fin.

High vorticity intensity, particularly at the tip of the canard, is undesired because the wing tip vortices could induce drag due to the downwash effect. To minimize the vorticity at the wing tip, winglet can be added and it can also significantly improve the aerodynamic characteristics of the flying body at the same time [43]. By using CFD approach, Babigian and Hayashibara revealed that winglet and raked wing tip design can be used to reduce the local vorticity magnitude. A clean wing configuration would increase the overall aspect ratio of the wing, thereby increasing the induced drag on it. Here, the usage of winglet would produce a force component in the thrust direction of the flying body and gathering the highly turbulent vortices flow behind the wing tip, thus minimizing the induced drag. Similar finding has also been made by Bojja and Garre [44], which their result justified that a blended winglet could yield the highest vorticity reduction effect than other winglet designs, such as the circular winglet. However, despite the benefits, the addition of winglet would increase the bending moment at the wing root, depending on the winglet design [45]. Therefore, the winglet should be carefully design as it may induce higher complexity and cost of construction of the wing.

The findings of the authors are summarized in Table 1.

TABLE 1: Comparison of Relevant CFD Findings from Various Authors.

No	Author	Geometry	Flow Model	Findings
1.	Al-Kayiem et al. [6]	Seamless Missile	Inviscid, Compressible	In-house code developed is capable to capturing the shock wave, indicating steep change in flow characteristics at supersonic speed.
2.	Kim et al. [7]	Canard Airplane	Inviscid, Compressible	Compared wind tunnel, flight data, DATCOM and CFD simulation results. DATCOM shows relatively poor agreement to the experimental result in terms of aerodynamic derivatives, $C_D$ and $C_N$ .
3.	Wee [8]	Canard Missile	SST $k - \omega$ , Compressible	SST $k - \omega$ yields a less accurate $C_D$ as compared to AP09 data.
4.	Zhang et al. [9]	Canard Missile	S-A Model, Compressible	In canard body, $C.P$ location did not vary much at low AOA.
5.	Tomi et al. [10]	Split-Canard Missile	SST $k - \omega$ , Incompressible	Pitching moment effect in split-canard lasts up to a higher AOA than single-canard, thus enhancing mid-air turning rate.
6.	Ridluan [11]	Seamless Missile	STD $k - \varepsilon$ , Compressible	Non-linearity increment for $C_N$ & $C_M$ and decrement for $C_D$ if AOA increases. Shock wave and vortices were visualized.
7.	Sahu et al. [12]	Seamless Missile with Microflap.	STD $k - \varepsilon$ , Compressible	Control forces and moments generated due to fin-body-microflaps shock interaction as compared to a normal seamless missile.
8.	Li et al. [13]	Streamlined Missile	S-A Model, Compressible	Simulated high subsonic speed using low speed wind tunnel with Karman-Tsien Correction, could yield a reasonably accurate results.
9.	Gulay et al. [14]	Seamless Missile, WAF and Flat Fin	$k - \varepsilon$ , $k - \omega$ & S-A Model, Compressible	Sum of rolling moment coefficient, $C_{RM}$ for WAF is the sum of $C_{RM}$ of the canted equivalent flat fins and the $C_{RM}$ due to fin's curvature.
10.	Zhang et al. [15]	Canard Body,	STD $k - \varepsilon$ , Compressible	At small AOA, aerodynamic characteristics of Canard-FSW depend

		FSW shape.		on the relative positions between canard and main wing. At large AOA, the characteristics depend also on the canard vortices feature.
11.	Xie et al. [16]	Canard Missile	S-A Model, Compressible	Aerodynamic characteristics depend on canard vortex and its effect on tail wing, which is sensitive to the canard thickness. Thinner canard produces weaker vortex, thus improves its stability quality.
12.	Kaleeswaran et al. [17]	Cruise Missile with Notched Canard	STD $k - \varepsilon$ , Compressible	Canard position and design affect its surface aerodynamic heating intensity. Excessive heating may damage the gravitational sensors on the canard. The proposed notched canard results in a lower temperature distribution on the canard, thus safer for the sensor.
13.	Anand et al. [18]	Canard-wing Configuration	SA-Model, Compressible	Vortices formation at the downstream of canard and interact with the main wing, thus affecting the flow field at that particular region.
14.	Cummings et al. [19]	Axisymmetric Afterbody	STD $k - \varepsilon$ , Compressible	The $k-\varepsilon$ model can predict the viscous features of a flow adequately, including shock wave, expansion fans and flow recirculating region.
15.	Shinde et al. [20]	Delta Wing	S-A Model, Compressible	The S-A Model is a suitable turbulence model to capture compressible viscous flow features. Vortices are formed at the wing surface at low AOA value and the vorticity intensity increases from apex to trailing edge of the wing.
16.	Sohail et al. [22]	Seamless Body	SST $k - \omega$ , Compressible	In supersonic flow, Euler method under-predicts the aerodynamic coefficients value while SST $k - \omega$ turbulent model achieves high agreement with the experimental results.



17.	Kwak et al. [23]	Wing-Body Configured Flying Body,	Different variations of the $k-\omega$ model and $q-\omega$ model	The variation of $k-\omega$ model has insignificant effect on aerodynamic characteristics. Both $k-\omega$ model and $q-\omega$ model shows good agreement with experimental results.
18.	Akgul et al. [24]	Canard Body	$k-\varepsilon$ Model, Compressible	The $k-\varepsilon$ model is more suitable in such analysis due to a relatively more accurate pitching moment value prediction as well as a faster solution converging time than the $k-\omega$ model. DATCOM approach over-predicted the value for $C_M$ of canard body.
19.	Luo et al. [25]	Ramped-cavity Flight Vehicle.	SST PANS & $k-\omega$ PANS	In PANS based model, variable $f_k$ model produce better agreement result to the RANS based model.
20.	Das et al. [26]	Cylindrical Afterbody	LES with Dynamic Smagorinsky Model	LES Model is able to predict large eddies formation and turbulent properties with higher accuracy as compared to RANS Model.
21.	Dahalan et al. [28]	Rocket & Projectile	N/A	The computer program based on USAF DATCOM produced a result with good agreement with experimental results.
22.	Kanamori and Suzuki [34]	Multiple Geometries	Inviscid, Compressible	Mathematical approach can be used to detect shock waves formation through the convergence of flow characteristics and then calculates the eigenvectors for the propagation velocity of the Riemann invariants.
23.	Nasir et al. [36]	Blended Wing Body	Wind Tunnel Simulation	The presence of canard reduces the $L/D$ ratio of the flying body. This could be improved by changing the main wing location forward instead of being at the very end of the main body.

24.	Zurriati et al. [37]	Blended Wing Body	Wind Tunnel Simulation	The canard highly influence the pitching moment coefficient, $C_M$ of the blended wing flying body, while the canard setting angle has little effect on the lift coefficient.
25.	Lopes et al. [38]	Wing-Canard Configuration	VSAERO Method	Additional lift force is produced at the canard. Therefore, design and location of the canard is emphasized as some applications do not desire excessive lift at the canard.
26.	Shi et al. [39]	Seamless Body of Chinned Fuselage	Wind Tunnel Testing	Fuselage vertical flow can delay the breakdown of main wing vortices and this effect could be weakened with angle of attack.
27.	Samimi et al. [40]	Canard Body With Delta Wing	Wind Tunnel Testing	In subsonic flow, the presence of canard postpones the vortex formation on the tail-fin.
28.	Giuni and Green [41]	Squared and Round Wing Tip	Wind Tunnel Testing	Squared wing-tip produces several primary vortex structures and accompanied by secondary vortex. Vortices behavior is steadier in round wing-tip with less intense secondary vortex.
29.	Davari et al. [42]	Wing-Body-Tail Configurations	Wind Tunnel Testing	Flow field structure at the main wing's downstream and tail-fin could be affected by main wing's aspect ratio, wing-to-tail span ratio and nose-body vortices interference.
30.	Babigian and Hayashibara [43]	Dihedral, Taper, and Sweep Wing	SA-Model, Compressible	Winglet and raked wing tip design can be used to reduce the local vorticity magnitude.
31.	Bojja and Garre [44]	Airfoil NACA 2213	N/A	Blended winglet yields the highest vorticity reduction effect than other winglet designs, such as the circular winglet.

## CHAPTER 3

### METHODOLOGY

This project will use two approaches to simulate 3D compressible flow field over seamless and canard body, which are CFD using ANSYS FLUENT and semi-empirical simulation using DATCOM. In present research, the aerodynamic flying bodies will be simulated at five different AOA ( $0^\circ$ ,  $2.5^\circ$ ,  $5^\circ$ ,  $7.5^\circ$ ,  $10^\circ$ ) at Mach 2.0.

### 3.1 CALCULATION

In this section, the relevant theories and calculations required for the CFD and DATCOM simulations will be presented.

#### 3.1.1 Operating Temperature and Pressure

The operating pressure and temperature change according to the elevation. These properties can be calculated using the relation in [6], as shown in Equation (1) to (2).

$$\text{Operating Temperature, } T_\infty = 288.16 - 0.0065H \quad (1)$$

$$\text{Operating Pressure, } P_\infty = 101,325 \left( \frac{T_\infty}{288.16} \right)^{\left( \frac{0.03415H}{288.16 - T_\infty} \right)} \quad (2)$$

By substituting  $H = 1,500$  m into Equation (1), an operating temperature,  $T_\infty$  of 278.4 K is obtained. After that, the  $H$  and  $T_\infty$  values are applied to Equation (2) to obtain an operating pressure of 84,643 Pa.

#### 3.1.2 Free Stream Velocity and Reynolds Number

In a supersonic air stream, the air is compressible and the speed of sound also varies according to the operating temperature. The speed of sound and free stream velocity in m/s at an altitude of 1500 m can be calculated using the relation in [46].

$$\text{Speed of Sound, } a = \sqrt{\gamma RT} = \sqrt{(1.4)(287)(278.4)} = 334.46 \text{ m/s}$$

$$\text{Free Stream Velocity, } V_\infty = Ma = 2(334.46) = 668.9 \text{ m/s}$$

On the other hand, Reynolds Number is the calculation for the ratio of inertia forces to viscous forces in a fluid flow [1]. Besides that, its value also indicates type of boundary layer forms on the surface of the flying body. The calculation with the air properties at an altitude of 1500 m is as shown below.

$$Re = \frac{\rho V L_{ref}}{\mu} = \frac{(1.0595)(668.9)(8.5)}{1.742 \times 10^{-5}} = 3.458 \times 10^8$$

where  $L_{ref}$  is the reference length of the flying body. Since the Reynold Number is of high value, the air flow over the flying body is supersonic and turbulent.

## 3.2 CFD SIMULATION

CFD simulation is the main approach to investigate the flow field and its resultant aerodynamic characteristics. It is divided into four main stages: Geometry Modeling, Mathematical Model Formulation, CFD Computational Grid Generation and Post-Processing and Validation.

### 3.2.1 Governing Equations

The present study of supersonic, compressible flow field over the seamless and canard body are governed by Reynolds-Average Navier-Stokes (RANS) Equation, a modified version of Navier-Stokes (NS) Equation specifically for turbulent flow [47].

The basis of the RANS Equation can be traced back to the NS Equation, where its continuity, momentum and energy equations for compressible and viscous flow are listed below. The following equations are in conservative and invariant form.

$$\text{Continuity:} \quad \frac{\partial \rho}{\partial t} + \nabla \cdot (\rho \mathbf{V}) = 0 \quad (3)$$

$$\text{Momentum:} \quad \frac{\partial}{\partial t} (\rho \mathbf{V}) + \nabla \cdot (\rho \mathbf{V} \mathbf{V}) = -\nabla p + \nabla \cdot \boldsymbol{\tau} + \mathbf{f} \quad (4)$$

$$\begin{aligned} \text{Energy:} \quad \frac{\partial}{\partial t} \left[ \rho \left( e + \frac{V^2}{2} \right) \right] + \nabla \cdot \left[ \rho \left( e + \frac{V^2}{2} \right) \mathbf{V} \right] \\ = \rho \dot{q} + \rho (\mathbf{f} \cdot \mathbf{V}) - \nabla \cdot (p \mathbf{V}) + \nabla \cdot (k \nabla T) + \dot{W}'_{viscous} \end{aligned} \quad (5)$$

where  $\rho$  is the air density,  $\mathbf{V}$  is the air velocity,  $p$  is pressure,  $\boldsymbol{\tau}$  is the deviatoric shear stress tensor,  $\mathbf{f}$  is the body forces acting on a control volume,  $e$  is internal energy,  $k$  is the thermal conductivity,  $T$  is temperature and  $\dot{W}'_{viscous}$  is the rate of work done

by frictional viscous forces [5, 48, 49]. The complete derivation of the NS Equations can be found in [5].

In turbulence modeling, Reynolds decomposition is introduced, where the instantaneous quantities are the function of a time-average quantities and fluctuating quantities. Equation (6) shows the Reynolds decomposition in terms of velocity. The concept here is to express the instantaneous velocity,  $u_i$  as a combination of time-average velocity,  $\bar{u}_i$  and fluctuating velocity,  $u'_i$ .

$$u_i = \bar{u}_i + u'_i \quad (6)$$

By applying the Reynolds decomposition into the continuity and momentum equation, the derivations give us the RANS Equations, as shown in Equation (7). In the equation, the derivative term of  $(-\rho\overline{u'_i u'_j})$  is the Reynolds Stress [47].

$$\frac{\partial \rho \bar{u}_i}{\partial t} + \frac{\partial \rho \bar{u}_i \bar{u}_j}{\partial x_j} = -\frac{\partial \bar{p}}{\partial x_j} + \frac{\partial}{\partial x_j} \left[ \mu \left( \frac{\partial \bar{u}_i}{\partial x_j} + \frac{\partial \bar{u}_j}{\partial x_i} - \frac{2}{3} \delta_{ij} \frac{\partial \bar{u}_m}{\partial x_m} \right) \right] + \frac{\partial}{\partial x_j} (-\rho \overline{u'_i u'_j}) \quad (7)$$

The present study will be using 2 Equations, Standard  $k - \varepsilon$  Turbulent Model to solve for the Reynold Stress. In  $k - \varepsilon$  model, the Reynolds Stress,  $(-\rho\overline{u'_i u'_j})$  can be expressed in terms of turbulent kinetic energy,  $k$  and turbulent dissipation,  $\varepsilon$ . The relationship between both variables is expressed in Equation (8) and (9). To solve  $k$  and  $\varepsilon$ , Closure approximation is used to form Equation (10) and (11) [47].

$$\mu_t = \rho C_\mu \frac{k^2}{\varepsilon} \quad (8)$$

$$-\rho \overline{u'_i u'_j} = \mu_t \left( \frac{\partial \bar{u}_i}{\partial x_j} + \frac{\partial \bar{u}_j}{\partial x_i} \right) - \frac{2}{3} \rho k \delta_{ij} \quad (9)$$

$$\frac{\partial k}{\partial t} + \bar{u}_j \frac{\partial k}{\partial x_j} = \frac{\partial}{\partial x_j} \left[ \frac{\partial k}{\partial x_j} \left( \nu + \frac{\nu_T}{\sigma_k} \right) \right] + \left[ \nu_T \left( \frac{\partial \bar{u}_i}{\partial x_j} + \frac{\partial \bar{u}_j}{\partial x_i} \right) - \frac{2}{3} \delta_{ij} k \right] \frac{\partial \bar{u}_i}{\partial x_j} - \varepsilon \quad (10)$$

$$\frac{\partial \varepsilon}{\partial t} + \bar{u}_j \frac{\partial \varepsilon}{\partial x_j} = \frac{\partial}{\partial x_j} \left( \frac{\nu_T}{\sigma_\varepsilon} \frac{\partial \varepsilon}{\partial x_j} \right) + C_{\varepsilon 1} \frac{\varepsilon}{k} \left[ \nu_T \left( \frac{\partial \bar{u}_i}{\partial x_j} + \frac{\partial \bar{u}_j}{\partial x_i} \right) - \frac{2}{3} \delta_{ij} k \right] \frac{\partial \bar{u}_i}{\partial x_j} - C_{\varepsilon 2} \frac{\varepsilon^2}{k} \quad (11)$$

$$\text{where} \quad \nu_T = C_\mu \frac{k^2}{\varepsilon} = \frac{\mu_t}{\rho} \quad (12)$$

In Equation (10), (11) and (12), the terms  $C_\mu$ ,  $C_{\varepsilon 1}$ ,  $C_{\varepsilon 2}$ ,  $\sigma_k$  and  $\sigma_\varepsilon$  are constant value and they vary according to the type of  $k - \varepsilon$  model being assumed. In Standard  $k - \varepsilon$  Turbulent Model, the values of those terms are expressed in Equation (13) [47].

$$C_\mu = 0.09, C_{\varepsilon 1} = 1.44, C_{\varepsilon 2} = 1.92, \sigma_k = 1.0, \sigma_\varepsilon = 1.3 \quad (13)$$

In this project, ANSYS FLUENT software will be used to solve RANS Equation for a solution of the flow field over seamless and canard body.

### 3.2.2 Geometry Modeling

The aerodynamic flying bodies' geometries as shown in Figure 2 are first modeled in SOLIDWORKS as a single part respectively. Then, the parts will be exported to STEP file for flow domain construction around the parts in ANSYS Geometry. Figure 4 shows the geometry of seamless and canard flying body drawn in SolidWorks 2011.



FIGURE 4: Seamless (Left) and Canard (Right) Body Geometry in SolidWorks.

The flow domain will be constructed in rectangular shape. Due to the axisymmetric nature of the flying bodies, the flow domain is modeled in half rectangular only. The far field boundary is placed at a large distance from the flying bodies to capture all necessary flow characteristics such as shock waves and wake turbulence around the flying body. In both axial and radial direction, the flow domain should be at least five times the length and ten times the diameter of the flying body.

As a result, a 110 m long, 50 m high and 25 m wide rectangular flow domain is constructed and fully enclosing the geometries. Upon modeling completion, the overall geometry will be meshed to form computational grid. Figure 5 shows the seamless flying body enclosed in the flow domain.

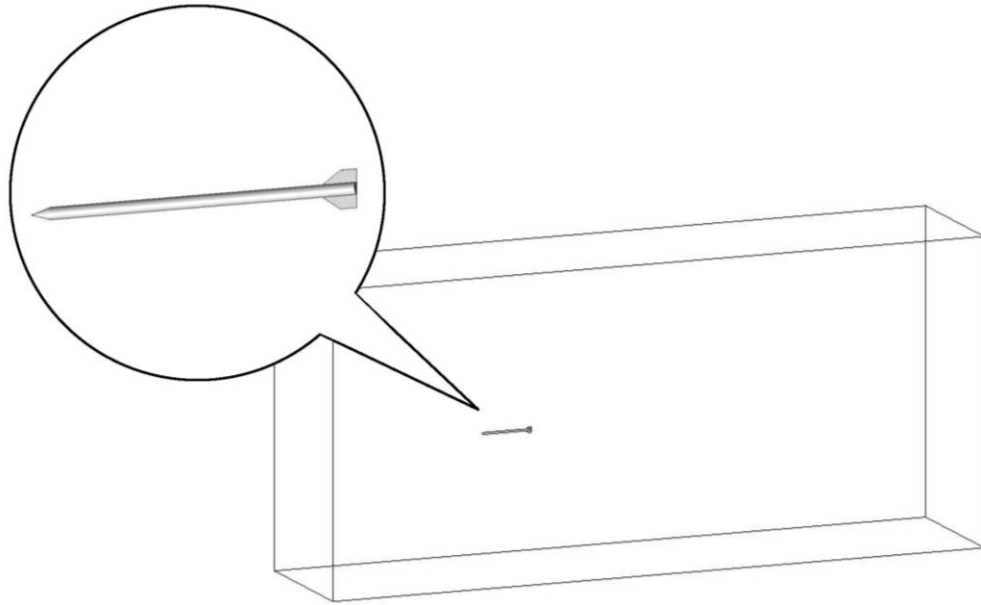


FIGURE 5: Seamless Body Enclosed in Flow Domain.

### 3.2.3 Computational Grid Generation for Seamless and Canard Body

The computational grid or mesh should be concentrated near the flying body's surface, whereas the mesh further away from it can be allowed to be relatively coarser to reduce the number of total mesh at that area, thus reducing the overall computing time. To resolve the viscous effect at the boundary layer region, inflation boundary layer function will be applied to the mesh. The skewness will be monitored to ensure as much meshes as possible are close to 0.

In order to choose a correct number of elements and sizes, mesh independency for the seamless and canard body has been studied and its results are documented in Appendices A, Table 9 to 10 and Table 12 to 13 respectively. The variation of drag coefficient,  $C_D$  with respect to the element number is also plotted in Figure 15 of Section 4.1.2- Seamless and Canard Flying Body. The parameters that are used in the final mesh generation are summarized in Table 11 and 14 in Appendices A, after it is justified by the mesh independency study.

Meanwhile, Figure 6 to 8 describe the mesh generated for seamless and canard body. Besides that, each surface of the flow domain has been named in order to define the boundary conditions in FLUENT. Figure 9 shows the flow domain geometry with named surface.

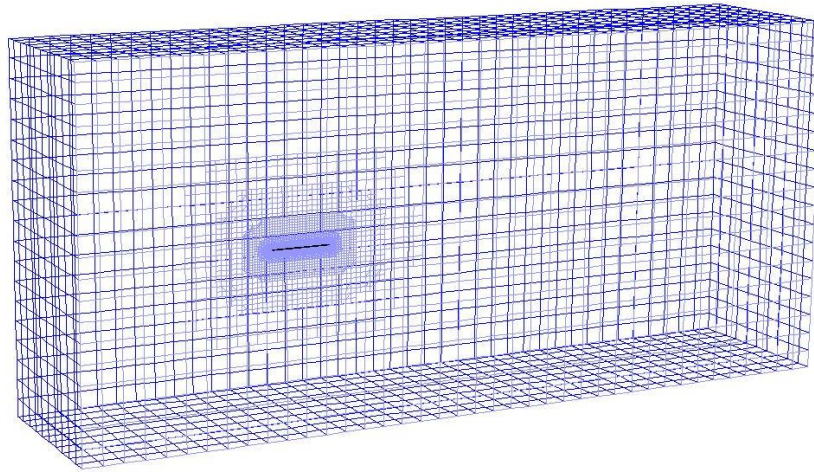


FIGURE 6: Overall Mesh of the Flow Domain for the Flying Body.

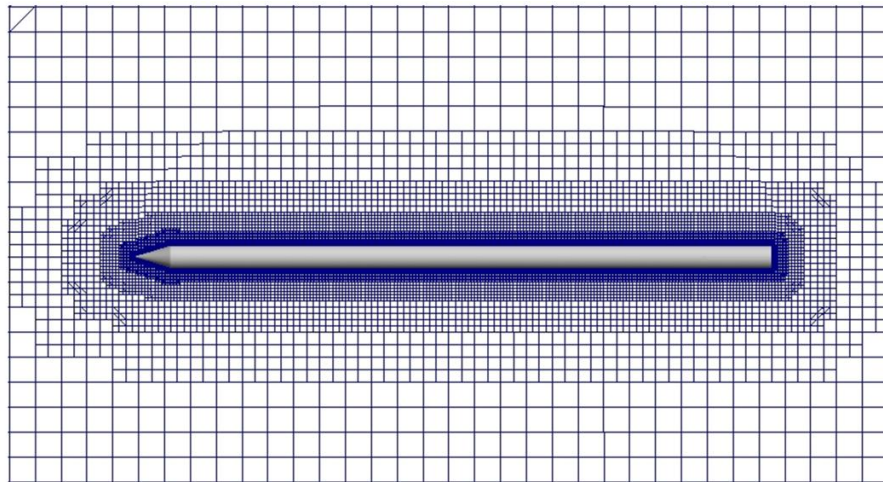


FIGURE 7: Close Up Mesh of the Seamless Body.

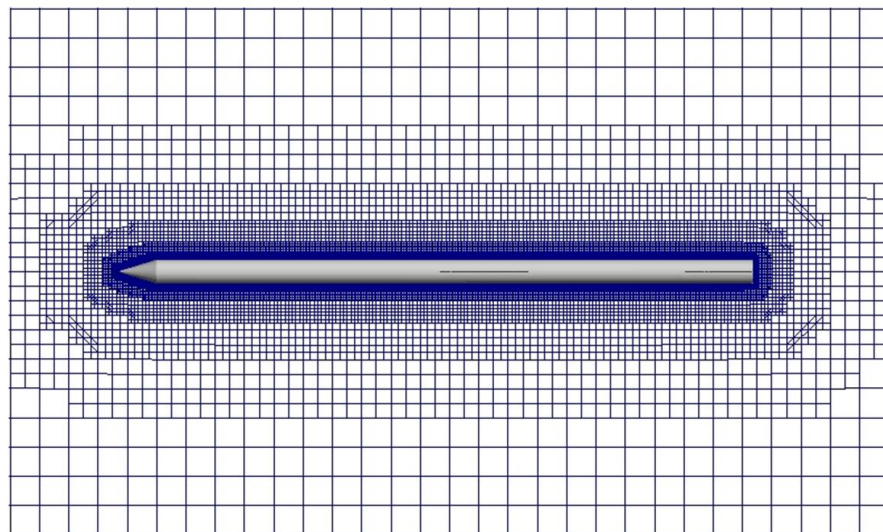


FIGURE 8: Close Up Mesh of the Canard Body.



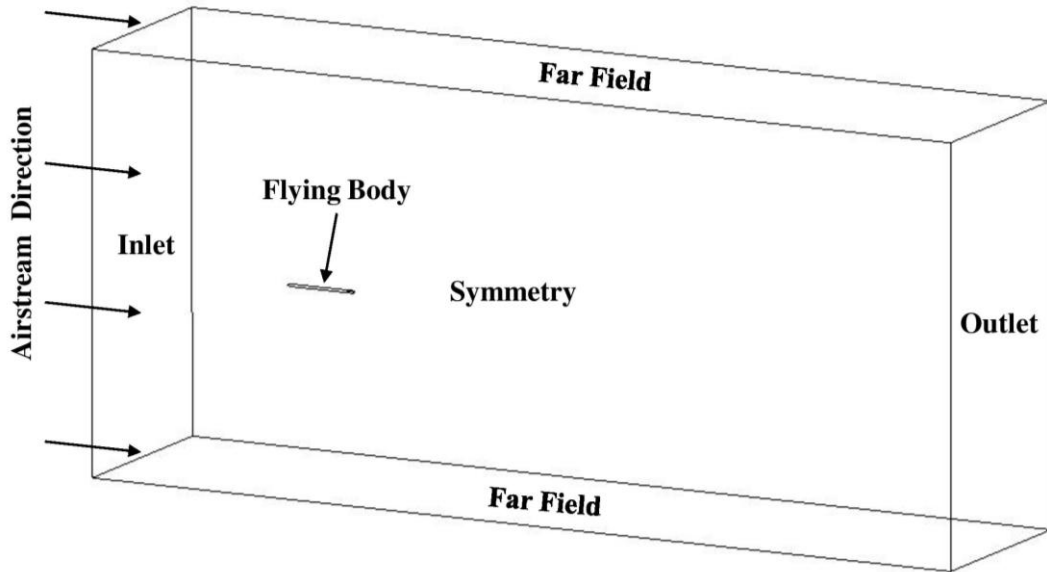


FIGURE 9: Flow Domain, Labeled With Named Surfaces.

### 3.2.4 CFD Flow Model Formulation

The flow field over the seamless and canard flying bodies will be modeled as turbulent flow. Therefore, ANSYS FLUENT is used to solve RANS equations. The viscous model to be used is Standard  $k - \varepsilon$  turbulent model. Air properties should be set to ideal-gas for compressible flow. All boundary of the flow domain, except for symmetry and flying body's surface, will be set as pressure-far-field boundary type. The velocity of the flow will be assigned to those boundary with its directional vector defined according to the AOA values. The compiled boundary conditions of named surface Inlet, Outlet and Far Field for each AOA value cases are documented in Table 15 in Appendices A. In order to validate that the boundary conditions are suitable for the simulation, a preliminary simulation on a slender body will be conducted using the exact boundary conditions in Table 2 and 15.

Scaled residual, lift and drag coefficient will be monitored to decide the convergence of the numerical solutions. To be considered as “converged”, the scaled residuals for Continuity should achieve below  $1 \times 10^{-4}$  while the other parameters, that are Velocities, Energy,  $k$  and  $\varepsilon$  should achieve below  $1 \times 10^{-6}$ . Besides that, the computed drag & lift coefficient should be stabilized at a constant value for at least 50 iterations.

TABLE 2: Boundary Conditions and Parameters of the Solver.

No.	Parameters	Settings
1	Type of Solver	Pressure-Based Solver.
2	Energy Equation	On.
3	Viscous Model	Two Equations, Standard $k - \varepsilon$ Turbulent Model.
4	Fluid Medium	Air as Ideal Gas.
5	Operating Altitude	1500 m.
6	Operating Pressure	84643 Pascal (Correspond to the Altitude).
7	Operating Temperature	278.4 K (Correspond to the Altitude).
8	Free Stream Velocity	Mach 2.0.
9	Reynolds Number	3.458E+008.
10	Reference Area	0.07354 m <sup>2</sup> .
11	Reference Length	8.5 m.
12	Reference Point for P. Moment Coefficient	Nose Tip of the Flying Body. Global Coordinate at X= 0; Y= 0; Z= 0.
13	Boundary Condition	<ul style="list-style-type: none"> <li>a. Inlet as Pressure Far-Field.</li> <li>b. Outlet as Pressure Far-Field.</li> <li>c. Symmetry as Symmetry.</li> <li>d. Flying Body as Wall.</li> <li>e. The Other 3 Surfaces as Pressure Far-Field.</li> </ul>

### 3.2.5 CFD Results Validation

The validation of the CFD results is conducted by evaluating the oblique shock wave parameters produced at the nose cone of the flying body. The evaluation of the shock waves of conical shape nose is more sophisticated than the conventional wedge-shape because of weaker shock at the cone and curved flow streamlines are formed over the cone surface. Such analysis can be done by numerically solving the Taylor-Maccoll Equation as shown in Equation (14) [1, 50, 51].

$$\frac{\gamma - 1}{2} \left[ 1 - V_r'^2 - \left( \frac{dV_r'}{d\theta} \right)^2 \right] \left[ 2V_r' + \frac{dV_r'}{d\theta} \cot \theta + \frac{d^2V_r'}{d\theta^2} \right] - \frac{dV_r'}{d\theta} \left[ V_r' \frac{dV_r'}{d\theta} + \frac{dV_r'}{d\theta} \left( \frac{d^2V_r'}{d\theta^2} \right) \right] = 0 \quad (14)$$

To solve Equation (14), the air stream velocity,  $M_\infty$  and shock wave angle  $\theta_s$  are pre-determined and they are used to find the flow deflection angle,  $\delta$ , velocity and shock wave,  $M$  using the oblique shock wave relation. Then, the nondimensional velocity,  $V'$  is calculated using Equation (15) and further resolved into radial velocity component,  $V'_r$  and polar velocity component,  $V'_\theta$  via Equation (16).

$$V' = \left[ \frac{2}{(\gamma - 1)M^2} + 1 \right]^{-1/2} \quad (15)$$

$$V' = \sqrt{(V'_r)^2 + (V'_\theta)^2} \quad (16)$$

The Taylor-Maccoll Equation can then be solved using numerical method with  $V'_r$  as the boundary value in steps of incremental angle,  $\Delta\theta$ , marching away from the shock boundary. In parallel,  $V'_\theta$  is computed using Equation (17) up to a point where  $V'_\theta = 0$  and this indicates that the  $\theta$  is equals to the conical half angle,  $\theta_c$ . The numerical computation of Equation (14) has been conducted by Anderson [1], Lassaline [50] and Feltham [51] and the results are commonly illustrated in the form of  $\theta_c$ - $\theta_s$ - $M$  diagram.

$$V'_\theta = \frac{dV'_r}{d\theta} \quad (17)$$

### 3.3 SEMI-EMPIRICAL SIMULATION

This simulation will be conducted to compare with the CFD results obtained from FLUENT. This simulation will be conducted in two stages, computation in Digital DATCOM program and result post-processing in MATLAB.

#### 3.3.1 Computation in USAF Digital DATCOM

The first approach is to write an input code to define the flight condition and geometries of the simulated flying body. The code will be written in Notepad and saved in input (.in) format.

Then, the input code will be opened in the DATCOM program and the resultant aerodynamic characteristics will be computed in a few seconds. The result is exported automatically in an output (.out) format file named datcom.out.

### 3.3.2 Result Post-Processing in MATLAB

In MATLAB, both input and output file from DATCOM can be viewed by using ‘type’ function. Besides that, the DATCOM output data can be assigned into MATLAB environment via ‘datcomimport’ command. Next, the result including aerodynamic coefficients will be listed in the Command Window. The computed aerodynamic coefficients can also be plotted in graphical form to examine the behavior of coefficients change against the AOA value.

### 3.4 PROJECT MANAGEMENT APPROACH

CFD and DATCOM simulations procedures have been discussed in detailed in Section 3.1 to 3.3. Hence, Figure 10 summarizes the step-by-step procedures in flow chart form.

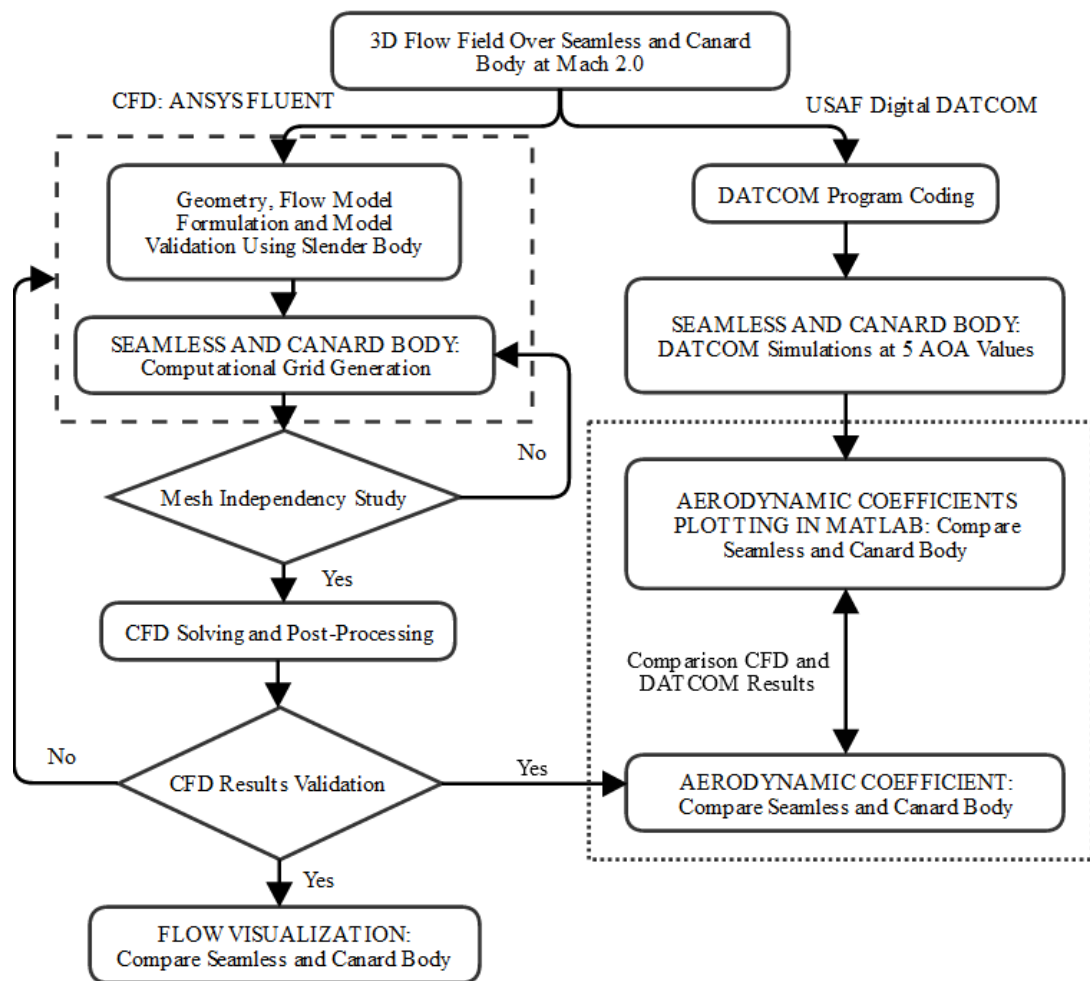


FIGURE 10: Process Flow of CFD and DATCOM Simulation.

Figure 10 shows that the compressible flow field over seamless and canard body is simulated using both CFD and DATCOM approach simultaneously, as presented in a flow chart format. One of the highlights in the flow chart is the procedure for the mesh independency study, where it continuously solve the numerical model until the quantitative solutions of the CFD approach converge and does not vary with further finer mesh. The CFD result is only considered valid when mesh independency has been achieved. The converged solution from CFD is then post-processed by integrating them to obtain aerodynamic coefficients and visualized to obtain the flow field structures. The aerodynamic coefficients will be compared to the DATCOM simulation result.

In this project, most of the time period will be allocated to the CFD and semi-empirical simulations. A period of four weeks has been allocated to seamless and canard body's simulations respectively. The timeframe for the remaining tasks are being monitored with a Gantt Chart, as presented in Table 3. In addition, Figure 11 describes the key milestones of this project and its expected time of completion.

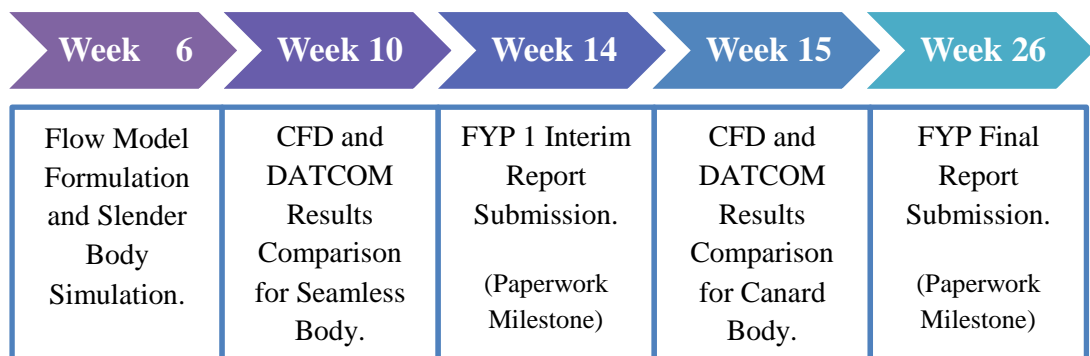


FIGURE 11: Project's Key Milestone.

Based on Figure 11 and Table 3, there are 5 key milestones that have been identified in the present study and they are highly feasible to be fulfilled within the given timeframe of 28 weeks. 3 of them will be required to be accomplished in the first 14 weeks of the project, which are the flow model formulation, completion of CFD and DATCOM simulations for seamless body along with Interim Report submission as part of the paperwork milestone. Likewise, additional 2 key milestones are expected to be achieved in the remaining 14 weeks, which are the completion of CFD and DATCOM simulations for canard body and the submission of Final Report.

TABLE 3: Gantt Chart and Key Milestones.

		Week																											
No.	Agenda	1	2	3	4	5	6	7	8	9	10	11	12	13	14	15	16	17	18	19	20	21	22	23	24	25	26	27	28
FYP 1																													
1.	Simulation Testing on Slender Body.	█	█																										
2.	Critical Literature Review.		█	█	█	█	█	█	█	█	█	█	█	█	█	█	█	█	█	█	█	█	█	█	█	█	█	█	█
3.	Flying Bodies' Geometrical Modelling.			█																									
4.	Cost Evaluation and Approval for Purchase (if any).			█	█	█																							
5.	Flow Model Formulation and Slender Body Simulation.				█	█	█	█	█	█	█																		
6.	CFD Simulation on Seamless Body.						█	█	█	█	█	█																	
7.	DATCOM Simulation on Seamless Body.						█	█	█	█	█	█																	
8.	CFD and DATCOM Results Comparison- Seamless Body.											█	█																
9.	CFD Simulation on Canard Body.											█	█	█	█	█													
10.	DATCOM Simulation on Canard Body.											█	█	█	█	█													
11.	FYP 1 Interim Report Submission.															█													
FYP 2																													
1.	CFD and DATCOM Results Comparison- Canard Body.																█	█											
2.	Aerodynamic Forces and Moment vs AOA Graph Plotting.																█	█	█										
3.	Flow Field's Contour and Vector Visualization.																█	█	█										
4.	Compare Results between Seamless and Canard Body.																	█	█	█	█								
5.	Interpret the Results and Write Discussion.																		█	█	█	█							
6.	Continue Project Works and Writing FYP Final Report.																				█	█	█	█	█				
7.	Technical Paper Writing and Submission.																								█	█	█	█	
8.	FYP Final Report Submission.																											█	
9.	VIVA.																												█
10.	Submission of Final Report Hard Bound Copy.																												█

● Represents Project's Key Milestones.

## CHAPTER 4

### RESULTS

#### 4.1 CFD RESULTS AND INTERPRETATION

##### 4.1.1 Slender Body

The geometry of the slender body resembles similarity of the nose region of the seamless and canard body. Therefore, the slender body is a useful approach to validate the boundary conditions, which will eventually be used for the actual CFD simulation of the flying bodies. The result is mainly validated by plotting the results in terms of air properties contour and examine the behavior of the shock wave formation, specifically the shock wave angle [6]. Besides the slender body, a similar validation approach will also be applied to the seamless and canard body in the following section. Figure 12 describes the dimensions and the mesh formulated for the slender body after it is justified by a mesh independency study as documented in Table 8 in Appendices A.

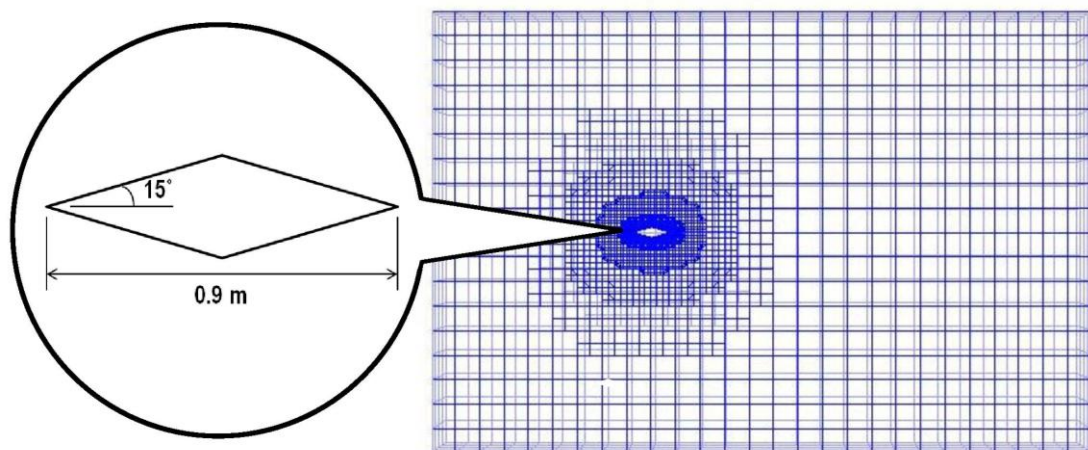


FIGURE 12: (Above) Dimensions of the Slender Body, (Bottom) Mesh of the Slender Body.

### a) CFD Simulations Results and Flow Model Validation

Figure 13 shows the flow field around the slender body at Mach 2.0 with zero AOA in the form of pressure, density, temperature and velocity contour.

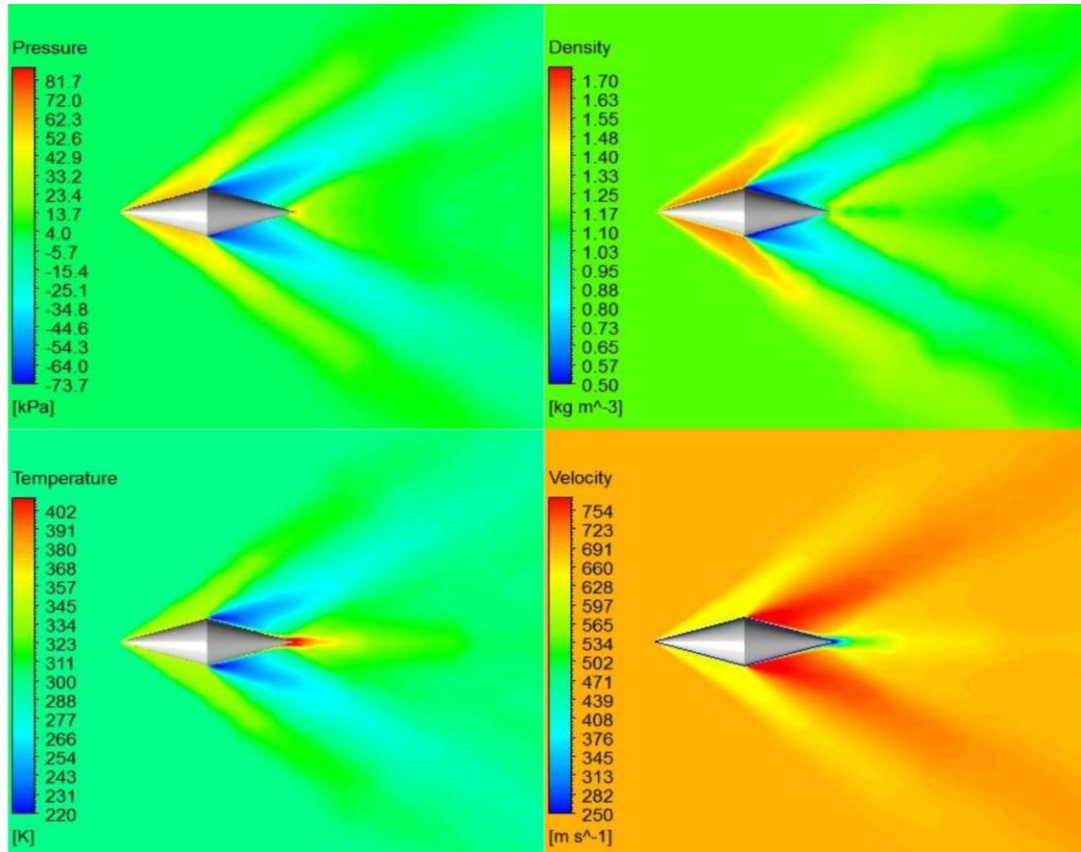


FIGURE 13: (From Top Left to Bottom Left, Clockwise) Contour of Static Pressure, Density, Velocity and Static Temperature for Slender Body.

In Figure 13, all 4 contours are characterized by the shock wave, which indicates the major change of air properties at the region due to flow travelling faster than the speed and sound, thus inducing a disturbance at the region. To validate that the CFD result is correct, the shock wave around the slender body is examined in terms of its half angle. The upstream half angle of the shock wave measured is approximately  $34^\circ$  based on the contour and the streamlined plotted. According to [1], the half angle of the shock wave is related to the half angle of the object body and free stream Mach number. Therefore, the measured half angle will be compared with the  $\theta_c$ - $\theta_s$ - $M$  Chart in [1], which is plotted based on numerical results of Equation (14) using Runge-Kutta method, as shown in Figure 14.



By using a nose cone half angle of  $15^\circ$  and a Mach number of 2.0, the theoretical shock wave angle obtained from the  $\theta_c$ - $\theta_s$ - $M$  Chart in Figure 14 is about  $33^\circ$  to  $34^\circ$  and it matched with the measured shock wave angle from the static pressure contour in Figure 13. For this reason, it is validated that the flow models formulated are suitable for the CFD simulation of the flying bodies and capable of producing an accurate result. Hence, a similar boundary condition will also be used for the flying bodies' simulations.

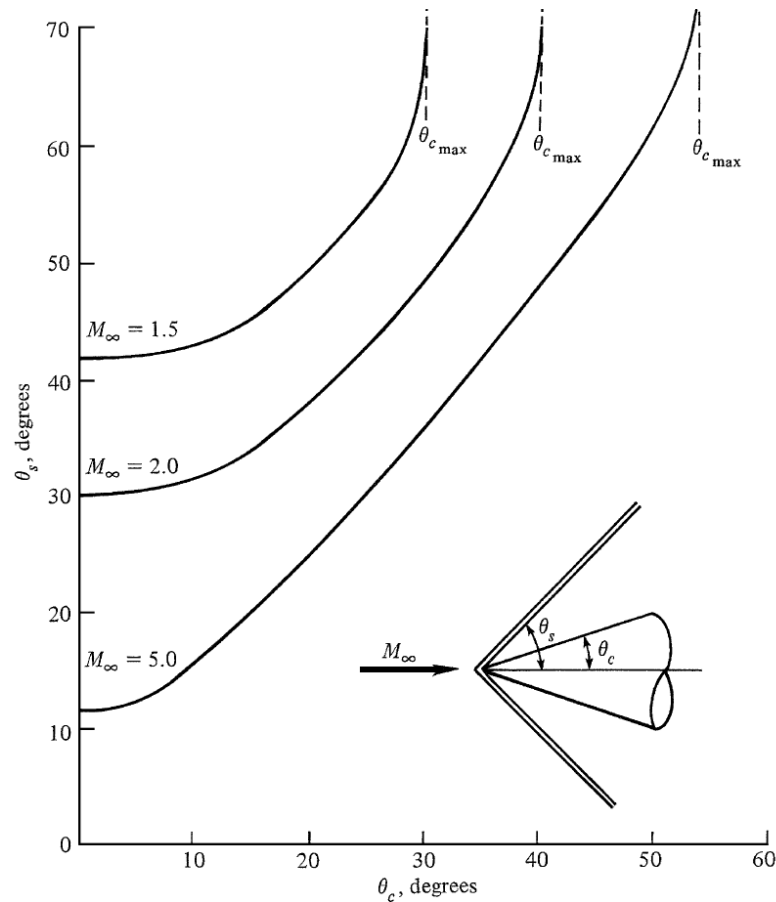


FIGURE 14: Theoretical Shock Wave Angle of Slender Body as Indicated in  $\theta_c$ - $\theta_s$ - $M$  Diagram [1].

#### 4.1.2 Seamless and Canard Flying Body

As discussed in Section 3.2.3- Computational Grid Generation for Seamless and Canard Body, the mesh independency study is conducted on both flying bodies from coarse to fine element sizes. Figure 15 shows the variation of the monitored variable, which is the drag coefficient,  $C_D$  of the seamless and canard body relative to the number of elements.

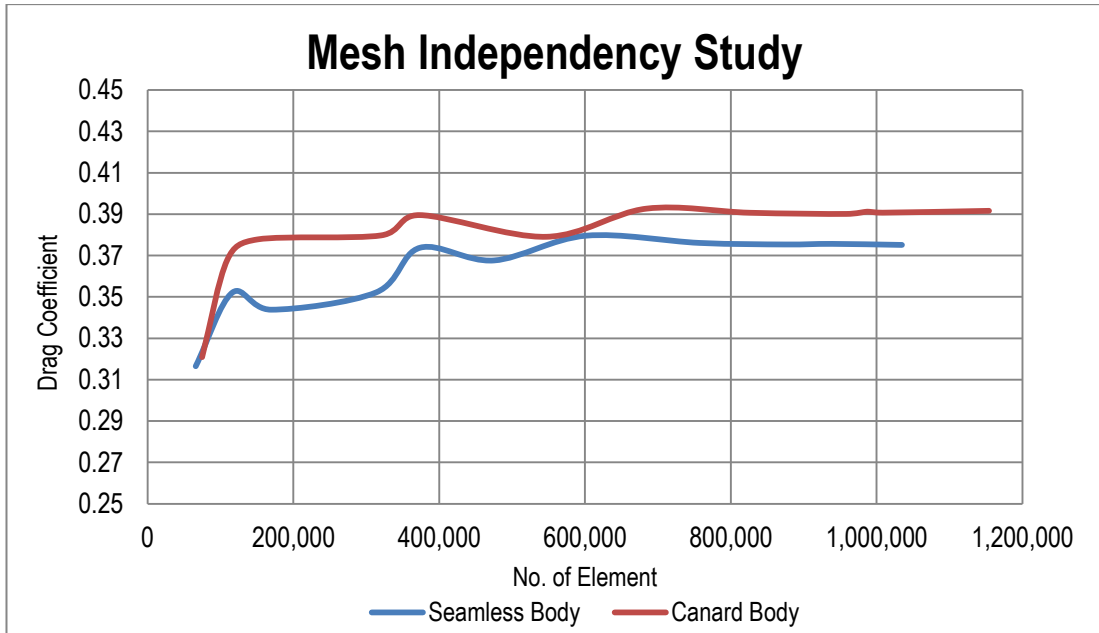


FIGURE 15:  $C_D$  variation vs Number of Element of Seamless and Canard Body.

Based on Figure 15, the  $C_D$  of both seamless and canard body varies and fluctuates in a wide range when the number of element is less than approximately 700,000. With the increment of element number, the  $C_D$  gradually stabilizes and will reach a state where the  $C_D$  will not be changing with a further finer mesh size. This state is known as mesh independency. The study suggests that the mesh independency will be achieved at 874,569 elements for seamless body and 1,008,302 elements for canard body.

#### a) CFD Simulation Results- Aerodynamic Coefficients

The generated mesh for seamless and canard body is then undergone CFD simulations at 5 different AOAs at a free stream of Mach 2.0. The simulations are assumed to be converged when the scaled residual drops below the convergence criteria and  $C_D$  does not significantly vary with further iterations. Figure 28 and 29 in Appendices A shows the sample scaled residual and  $C_D$  plot of CFD simulation for seamless body at AOA of  $0^\circ$  and Mach number of 2.0.

The solutions obtained from the simulations are then post-processed to acquire the aerodynamic coefficients for each AOA cases. Table 4 and 5 compile the CFD aerodynamic coefficients,  $C_D$ ,  $C_L$ ,  $C_A$ ,  $C_N$  and  $C_M$  of the seamless and canard body respectively.

TABLE 4: Aerodynamic Coefficients for Seamless Body, CFD.

Angle of Attack	Drag, $C_D$	Lift, $C_L$	Axial, $C_A$	Normal, $C_N$	P. Moment, $C_M$
0°	0.328	0	0.328	0	0
2.5°	0.344	0.401	0.326	0.416	0.337
5°	0.410	0.842	0.335	0.875	0.700
7.5°	0.509	1.292	0.336	1.347	1.057
10°	0.649	1.747	0.336	1.833	1.403

TABLE 5: Aerodynamic Coefficients for Canard Body, CFD.

Angle of Attack	Drag, $C_D$	Lift, $C_L$	Axial, $C_A$	Normal, $C_N$	P. Moment, $C_M$
0°	0.391	0	0.391	0	0
2.5°	0.415	0.567	0.390	0.584	0.391
5°	0.491	1.238	0.381	1.276	0.875
7.5°	0.637	1.967	0.375	2.033	1.410
10°	0.871	2.710	0.387	2.820	1.959

As a comparison, a DATCOM simulation is computed using the similar flight parameters and operating conditions as the CFD. A DATCOM Input Code is first written in Notepad and then simulation was executed and imported into MATLAB for data tabulation. Table 6 and 7 compile the aerodynamic coefficients of seamless and canard body respectively, resulted from DATCOM simulation.

TABLE 6: Aerodynamic Coefficients for Seamless Body, DATCOM.

Angle of Attack	Drag, $C_D$	Lift, $C_L$	Axial, $C_A$	Normal, $C_N$	P. Moment, $C_M$
0°	0.324	0	0.324	0	0
2.5°	0.336	0.388	0.319	0.403	0.323
5°	0.393	0.991	0.305	1.022	0.802
7.5°	0.522	1.724	0.293	1.777	1.421
10°	0.756	2.668	0.281	2.759	2.185

TABLE 7: Aerodynamic Coefficients for Canard Body, DATCOM.

Angle of Attack	Drag, $C_D$	Lift, $C_L$	Axial, $C_A$	Normal, $C_N$	P. Moment, $C_M$
0°	0.348	0	0.348	0	0
2.5°	0.373	0.725	0.341	0.74	0.536
5°	0.469	1.571	0.331	1.606	1.074
7.5°	0.671	2.413	0.350	2.480	1.620
10°	1.005	3.420	0.396	3.542	2.181

Meanwhile, Figure 30 and 31 in Appendices A shows the DATCOM results of seamless and canard body respectively in the MATLAB interface, along with the DATCOM code for both seamless and canard body in subsection 3 of Appendices A. With both CFD and DATCOM results obtained, the aerodynamic coefficients,  $C_D$ ,  $C_L$ ,  $C_A$ ,  $C_N$  and  $C_M$  are plotted against the AOA values, as shown in Figure 16 with seamless body on the left column and canard body on the right column.

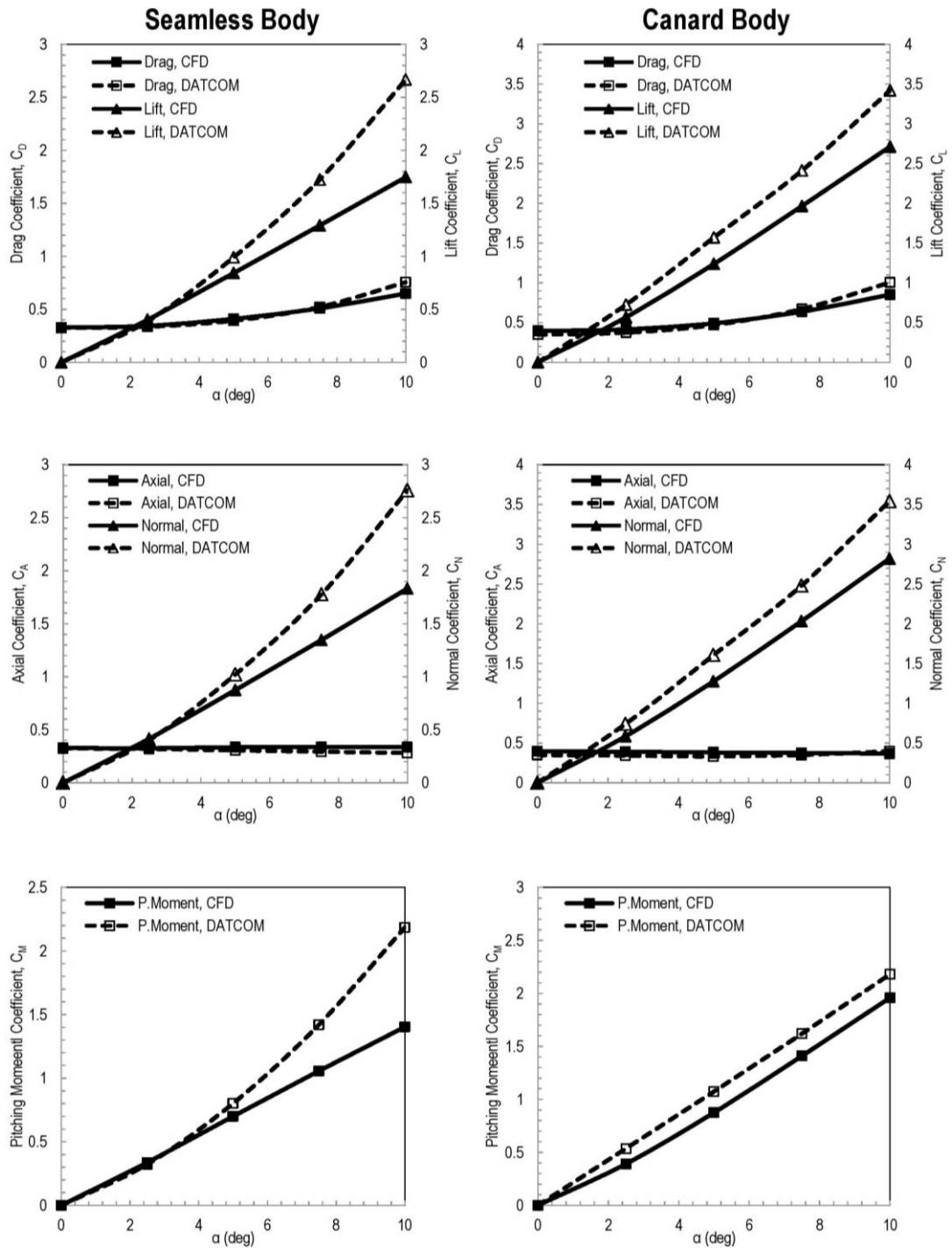


FIGURE 16: Aerodynamic Coefficients of Seamless (Left) and Canard (Right) versus Angle of Attack.

Based on Figure 16, lift,  $C_L$ , normal,  $C_N$  and moment,  $C_M$  coefficient, for both CFD and DATCOM is highly proportional to the angle of attack while the axial coefficient,  $C_A$  does not vary much with the angle of attack. Similarly, drag coefficient,  $C_D$  also show proportionality to the angle of attack but at a lower gradient. A similar relationship between the coefficients and angle of attack was presented in [8, 9, 13].

Next, the results between CFD and DATCOM are compared. In Figure 16, the CFD Result is represented in solid line while the DATCOM Result in dashed line. In terms of  $C_A$  and  $C_D$ , both results show relatively good agreement with small error for both seamless and canard body. However, the DATCOM over predicted the value for  $C_L$ ,  $C_N$  and  $C_M$ , therefore showing a lower agreement with the CFD result. For those 3 coefficients predicted by DATCOM, seamless body yields a larger error with non-linearity as compared to the canard body. The phenomenon of having an inaccurate  $C_N$  and  $C_M$  prediction by DATCOM software also happened in some researches done previously, such as by Ridluan [11] and Maurice [29], where  $C_N$  was also inaccurately-predicted by the DATCOM. In their cases, they proposed to derive an error correction factor to adjust the  $C_N$  and  $C_M$  value closer to the CFD and experimental value. Those factors are specific and it could be varied according to the different shape of the geometry.

Since the  $C_D$  and  $C_L$  are also related to both  $C_N$  and  $C_A$ , the under-prediction of  $C_N$  by DATCOM also cause a certain degree of offset from CFD Result in terms of  $C_D$  and  $C_L$ , as shown in Figure 16. The relationship between  $C_D$ ,  $C_L$ ,  $C_A$  and  $C_N$  are expressed in Equation (18) and (19).

$$C_L = C_N \cos \alpha - C_A \sin \alpha \quad (18)$$

$$C_D = C_N \sin \alpha + C_A \cos \alpha \quad (19)$$

In Equation (18),  $C_L$  is the function of  $C_N \cos \alpha$  and  $C_A \sin \alpha$ . Here,  $\cos \alpha$  will result in a higher value than  $\sin \alpha$ , therefore the influence of  $C_N$  offset will induce a larger error in  $C_L$ . On the other hand,  $C_D$  is less influenced by the error in  $C_N$  based on Equation (19). Besides that, the error could also be due to the limitation usage of NACA airfoil in DATCOM, which slightly differs from the actual fin's section of the seamless body.

Furthermore, the lift to drag ( $L/D$ ) coefficient ratio can be calculated by dividing the lift coefficient,  $C_L$  by drag coefficient,  $C_D$  as shown in Figure 17.

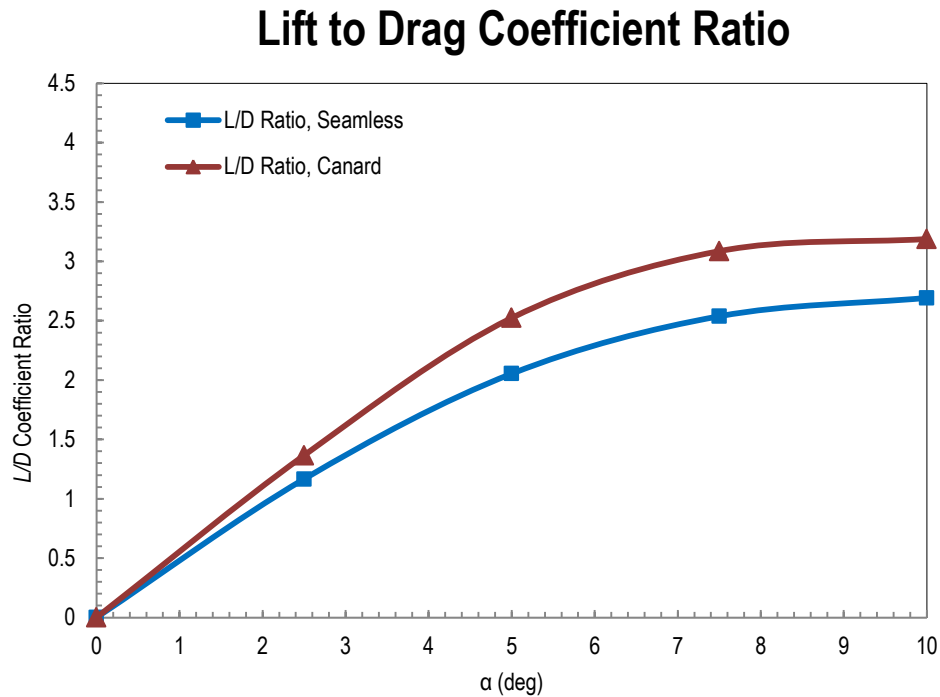


FIGURE 17: Lift to Drag Coefficient Ratio of Seamless and Canard Body

Based on Figure 17, it is observed that the addition of canard onto a flying body will increase its  $L/D$  coefficient ratio. In this study, the canard body yields a higher  $L/D$  ratio than the seamless body by approximately 20%. This observation justifies that despite a higher  $C_D$  due to canard configuration, the lift force generated by the canard is more than sufficient to compensate the increased drag force. Therefore, a satisfying lifting performance can be achieved by the canard configured body as compared to a seamless body.

In overall, the aerodynamic coefficient of the canard body predicted by CFD and DATCOM has presented a higher value as compared to the seamless body. Significant effect of canard can be observed especially in terms of  $C_L$  and  $C_N$  which could be increased by approximately 54%. The canard also contributes a higher  $C_D$ ,  $C_A$  and  $C_M$  by a range of 20% to 40% more as compared to a seamless body. A relatively good agreement is observed in  $C_D$  and  $C_A$  while  $C_L$ ,  $C_N$  and  $C_M$  are being over-predicted by DATCOM.  $L/D$  ratio also increases by approximately 20% in the canard body.

### b) CFD Simulation Results- Flow Field

The solutions for CFD for each AOA cases are plotted in contour form for four main parameters, which are 1) Static Pressure, 2) Temperature, 3) Density and 4) Velocity. By having the flow field visualized, the shock wave formations and vortices behavior can be examined and validated if the solutions are accurate. They are presented in Figure 18, 19, 20 and 21, with the left column as seamless body and the right column as canard body. The shock wave angle measured from the contour is approximately  $35^\circ$ . By evaluating the relationship between shock wave angle and nose cone angle using Taylor-Maccoll Equation and  $\theta_c$ - $\theta_s$ - $M$  Diagram [1, 50, 51], a good agreement between them is observed, hence the CFD results are validated.

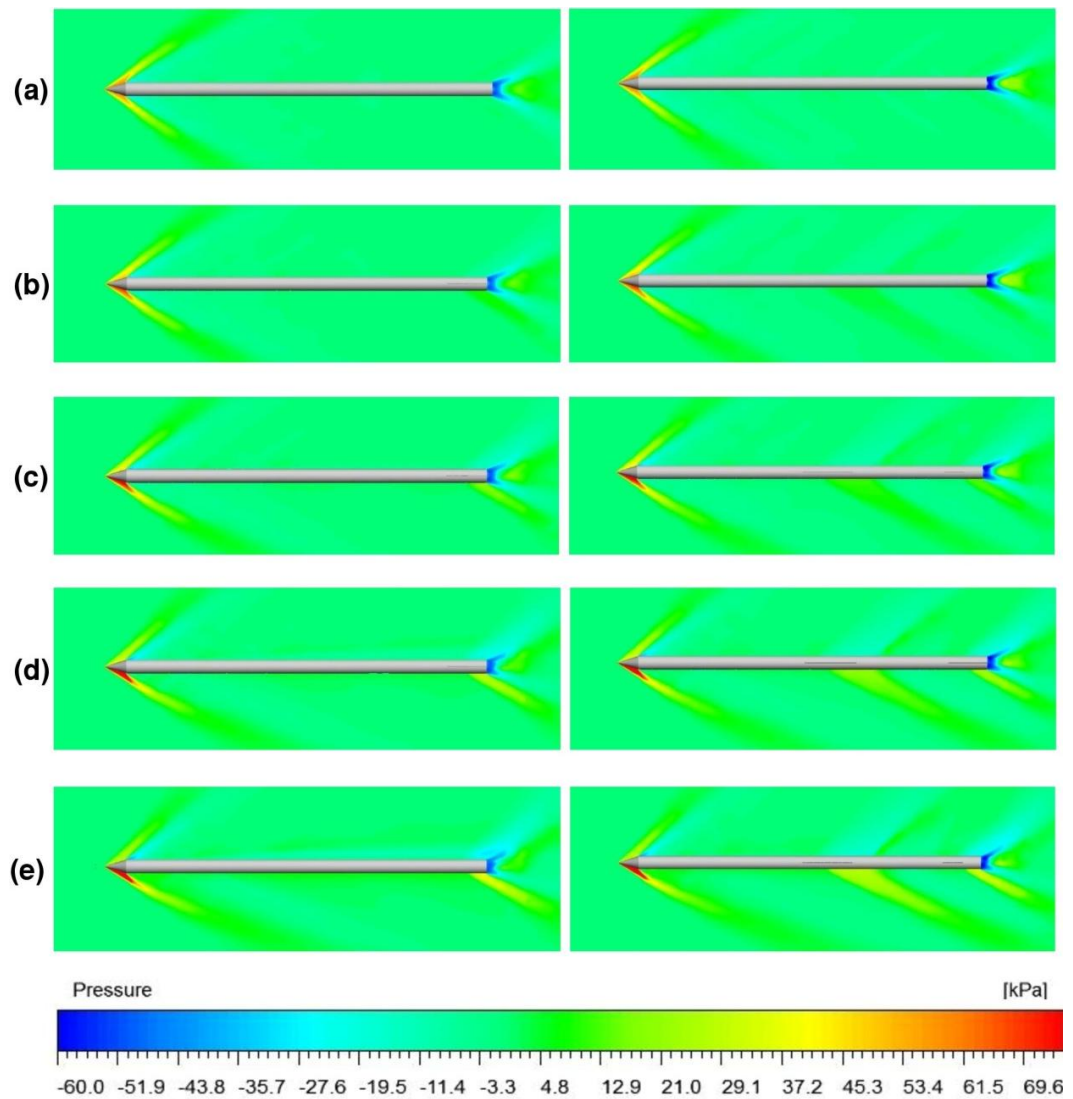


FIGURE 18: Pressure Contour Showing the Shock Wave of Seamless (Left) and Canard (Right) at (a) AOA  $0^\circ$ , (b) AOA  $2.5^\circ$ , (c) AOA  $5.0^\circ$ , (d) AOA  $7.5^\circ$  and (e) AOA  $10.0^\circ$ .

As predicted prior to the simulations, the shock wave angles of the upper and lower half of the flying bodies will change with respect to the AOA. When the AOA increases, the upper shock wave angle increases while the lower shock wave angle decreases, as illustrated from Figure 18. A similar phenomenon has also been documented in the finding by Akgul et al. [24]. An additional shock wave is also observed to be propagating from the leading edge of the canard in canard body. At the same time, the wake formation at the rear region of the flying body also tends to shift upwards relative to the longitudinal axis line of the body when the AOA values increases. A low pressure region also started to develop, as indicated in light-blue color contour on the upper region of the bodies when the AOA is increased to  $10^\circ$ .

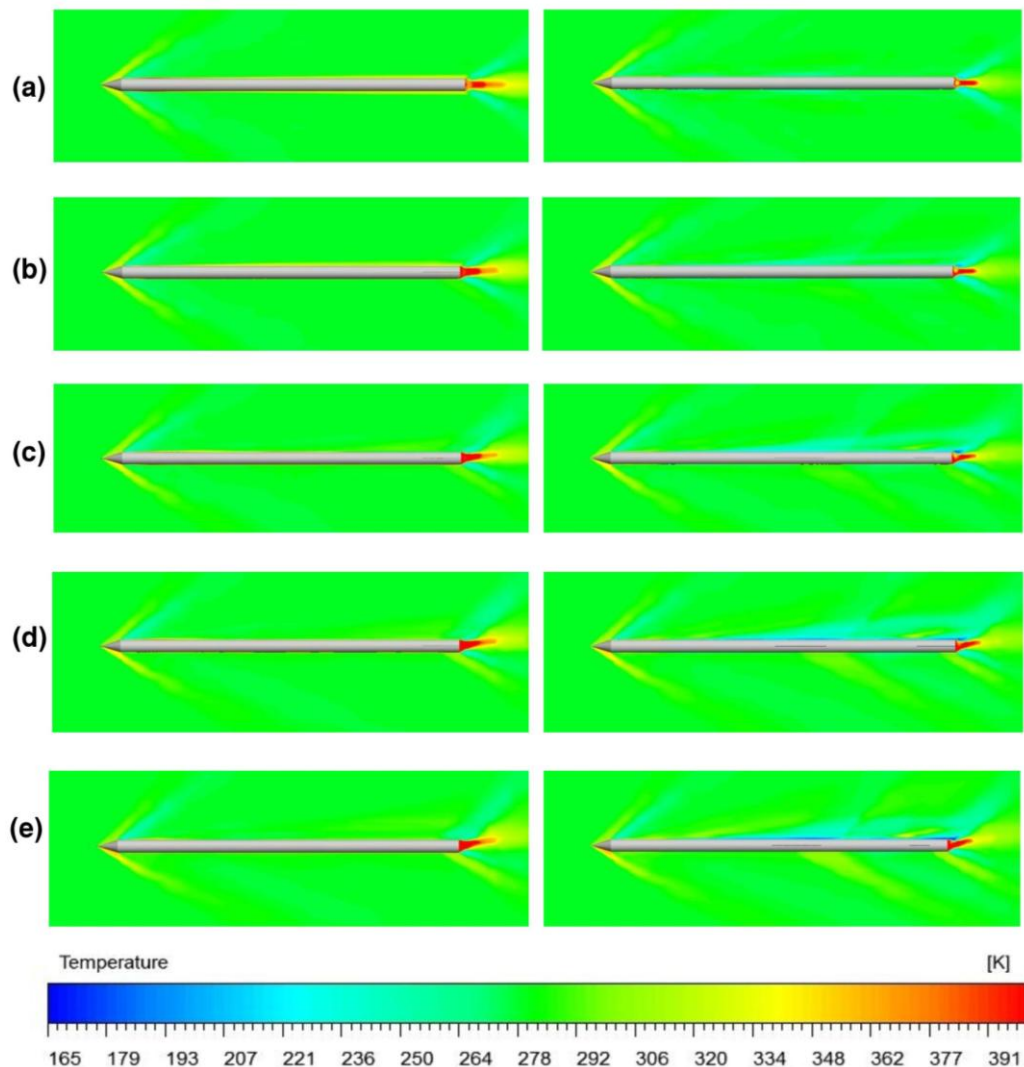


FIGURE 19: Temperature Contour Showing the Shock Wave of Seamless (Left) and Canard (Right) at (a) AOA  $0^\circ$ , (b) AOA  $2.5^\circ$ , (c) AOA  $5.0^\circ$ , (d) AOA  $7.5^\circ$  and (e) AOA  $10.0^\circ$ .



In Figure 19, the temperature contour reveals that the upper surface of the seamless body is at a higher temperature than the canard body. It is observed that the contour above the seamless body is on a higher temperature of yellowish-red, than the one in canard body, which is bluish in colour. A region of low temperature, specifically lower than the operating temperature of 278.4 K, also forms above the canard body. This low temperature region expands larger with respect to the AOA. In details, a surface temperature contour is plotted and will be explained in Figure 24 of the following sections. Similarly, the temperature contour reveals a series of shock wave along the body and the shock wave angle change over the increment of AOA.

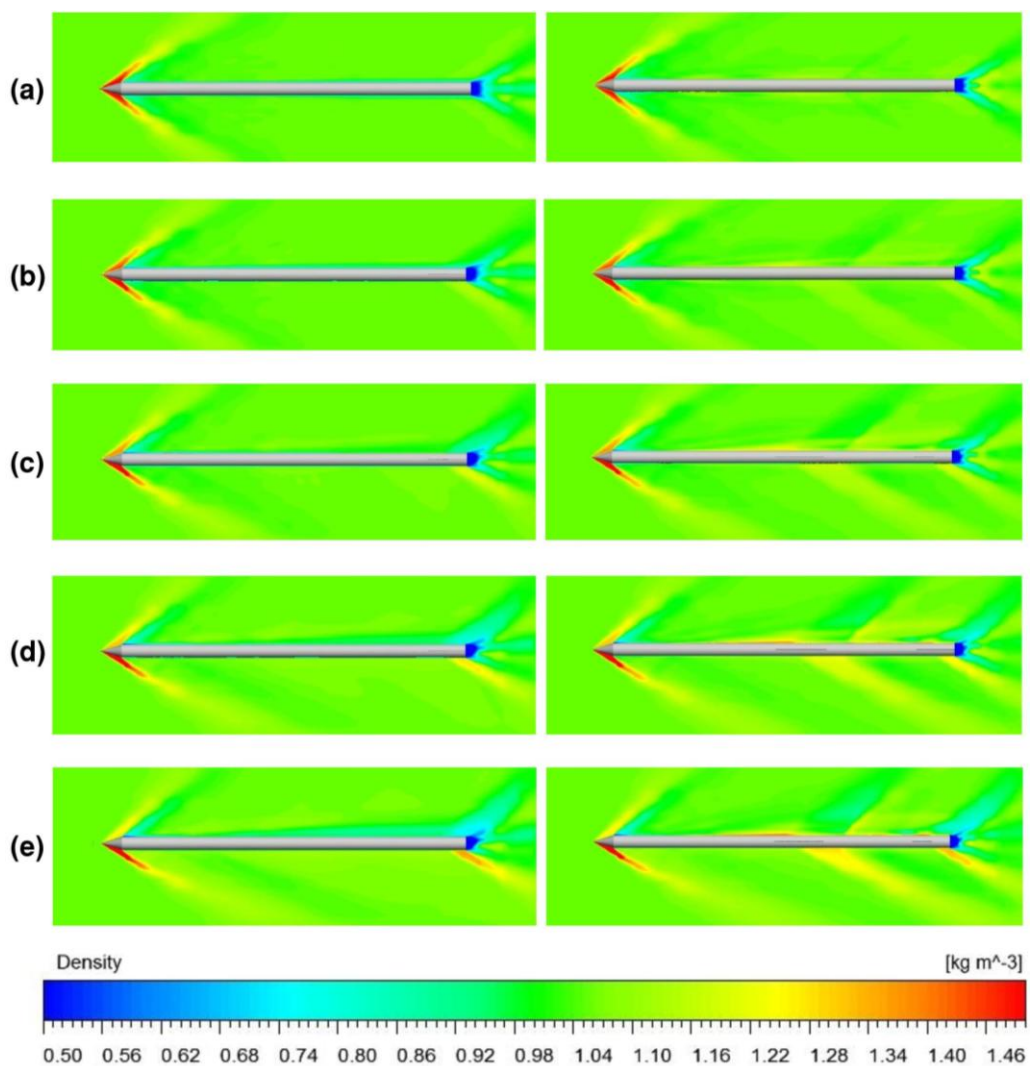


FIGURE 20: Density Contour Showing the Shock Wave of Seamless (Left) and Canard (Right) at (a) AOA 0°, (b) AOA 2.5°, (c) AOA 5.0°, (d) AOA 7.5° and (e) AOA 10.0°.

In Figure 20, the density distribution of both seamless and canard body is almost similar, except there is a region of higher density air accumulated at the canard area

in the canard body. Such phenomenon could be due to the existence of stagnation point, which is the leading edge of the canard. Furthermore, the air density around the canard is observed to be increasing over the increment of AOA values. In contrast, the low density region which is formed above the seamless body expanded into a larger area relative to the AOA. Here, it can be seen that the existence of canard in a flying body impacts the air density variation of the region in a completely opposite way and its effect becomes obvious when the AOA is larger than  $0^\circ$ .

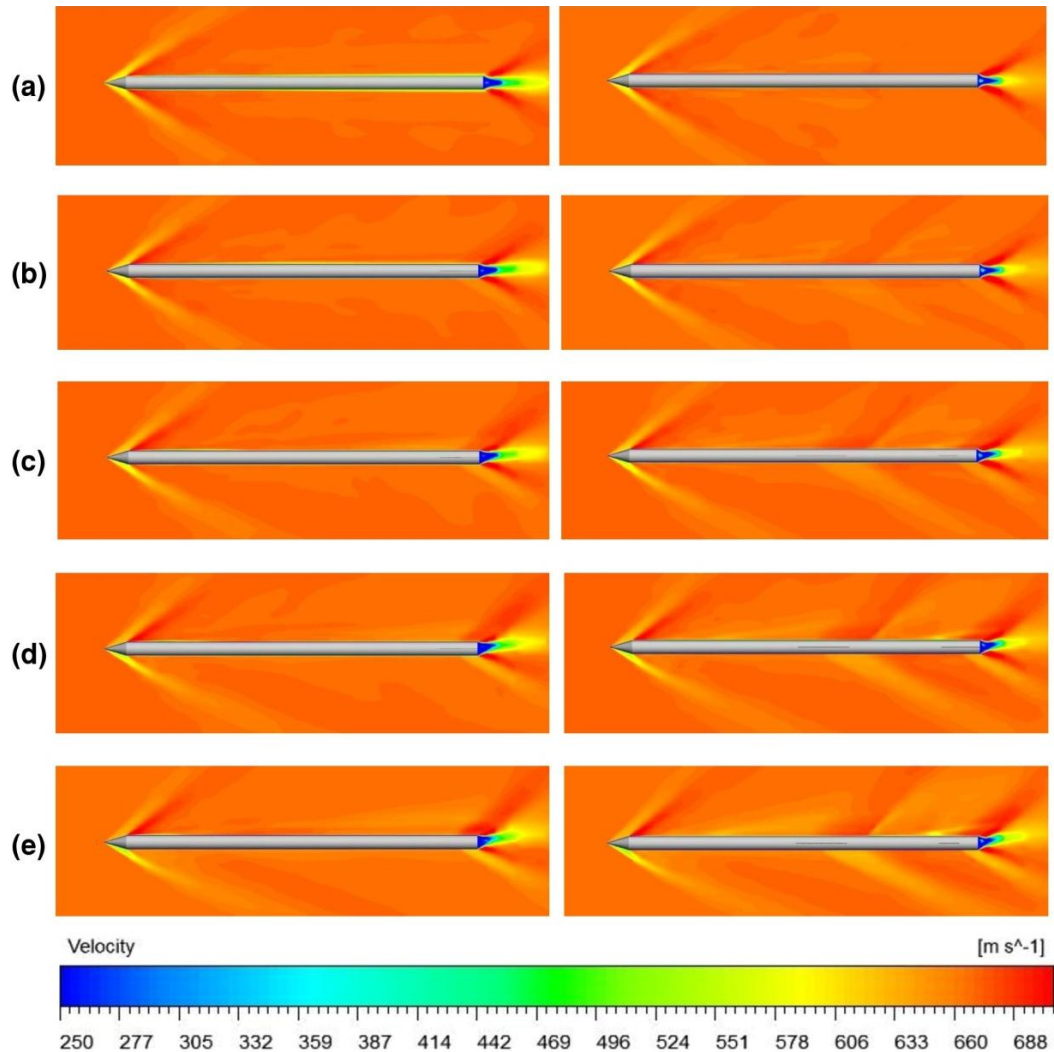


FIGURE 21: Velocity Contour Showing the Shock Wave of Seamless (Left) and Canard (Right) at (a) AOA  $0^\circ$ , (b) AOA  $2.5^\circ$ , (c) AOA  $5.0^\circ$ , (d) AOA  $7.5^\circ$  and (e) AOA  $10.0^\circ$ .

Figure 21 shows additional shock wave formation from the canard region. The air velocity also decreases across the shock wave as the contour shows a lighter color in the shock wave area than the free stream area, while still remaining at supersonic speed. Comparing Figure 18 to 21, it is observed that inside the oblique shock wave,

the pressure, temperature and density of air increase while the air velocity decreases. This denotes the enthalpy of air across the shock wave increases and subsequently decreasing its velocity as the total enthalpy should remain unchanged between the free stream and within the shock wave, as documented in the shock wave relation [1].

Next, to achieve higher details, Figure 22 compares the pressure contour between seamless and canard body in 3 dimensional at  $x = 0.5$  m,  $5.5$  m and  $8.5$  m at  $10^\circ$  of AOA. This comparison further justify the observation where  $C_L$  is higher in canard body than seamless body. In Figure 22, at  $x = 5.5$  m, a large pressure difference is detected at the trailing edge of the canard whereas only a small pressure difference forms in seamless body at that same location. As a whole, by comparing the pressure contour between seamless and canard body in Figure 18 and 22, it is observed that an additional shock wave is formed and a low pressure region is developed at the top surface of the canard, whereby such phenomenon does not happen in the seamless body due to the absence of canard. This low pressure region contributes to a pressure difference and subsequently forms an additional lift force, thereby justifying the findings where a higher  $C_L$  is obtained in the canard body.

The pressure and temperature distribution on the top surface of seamless and canard are also plotted in Figure 23 and 24 respectively. The results in Figure 23 and 24 will be used to justify and compare with the findings in Figure 18 and 19 of the previous sections. Figure 23 reveals that the pressure on the nose cone is reduced for both bodies when the angle of attack is increased. A relatively low pressure region is formed after the nose cone and gradually propagates further downstream relative to the AOA value. This phenomenon could be due to the change of angle between the upper oblique shock wave and the body's longitudinal axis. Besides that, significant low pressure regions are observed at the tail-fin and canard. With the presence of canard, the pressure at the top surface of the tail-fin is slightly higher than the seamless body, thereby losing a small amount of lift force due to a lower pressure difference. However, the significant pressure difference on the canard compensates the lost lift, which yields a higher lift force coefficient than seamless body in return.

Based on Figure 24, the temperature distribution is largely different between both bodies. A relatively high temperature is developed in stagnation area, such as the nose tip and leading edge of the tail-fin and canard, as an effect of aerodynamic

heating. The main body of the seamless body is at a higher temperature than the canard body in overall. In seamless body, the temperature on the main body rises while the tail-fin decreases relative to the AOA. A significant low temperature area is also observed at its wing tip. Contrarily, the main body of the canard body is mostly at a lower temperature than the ambient temperature of 278.4 K. High temperature region is found at the wing tip of canard and also at near the wing root of the tail-fin. As the canard and tail-fin share the same wing span, this could be due to the downwash from canard which heavily influences the air properties at its downstream, thereby changing the local temperature intensity.

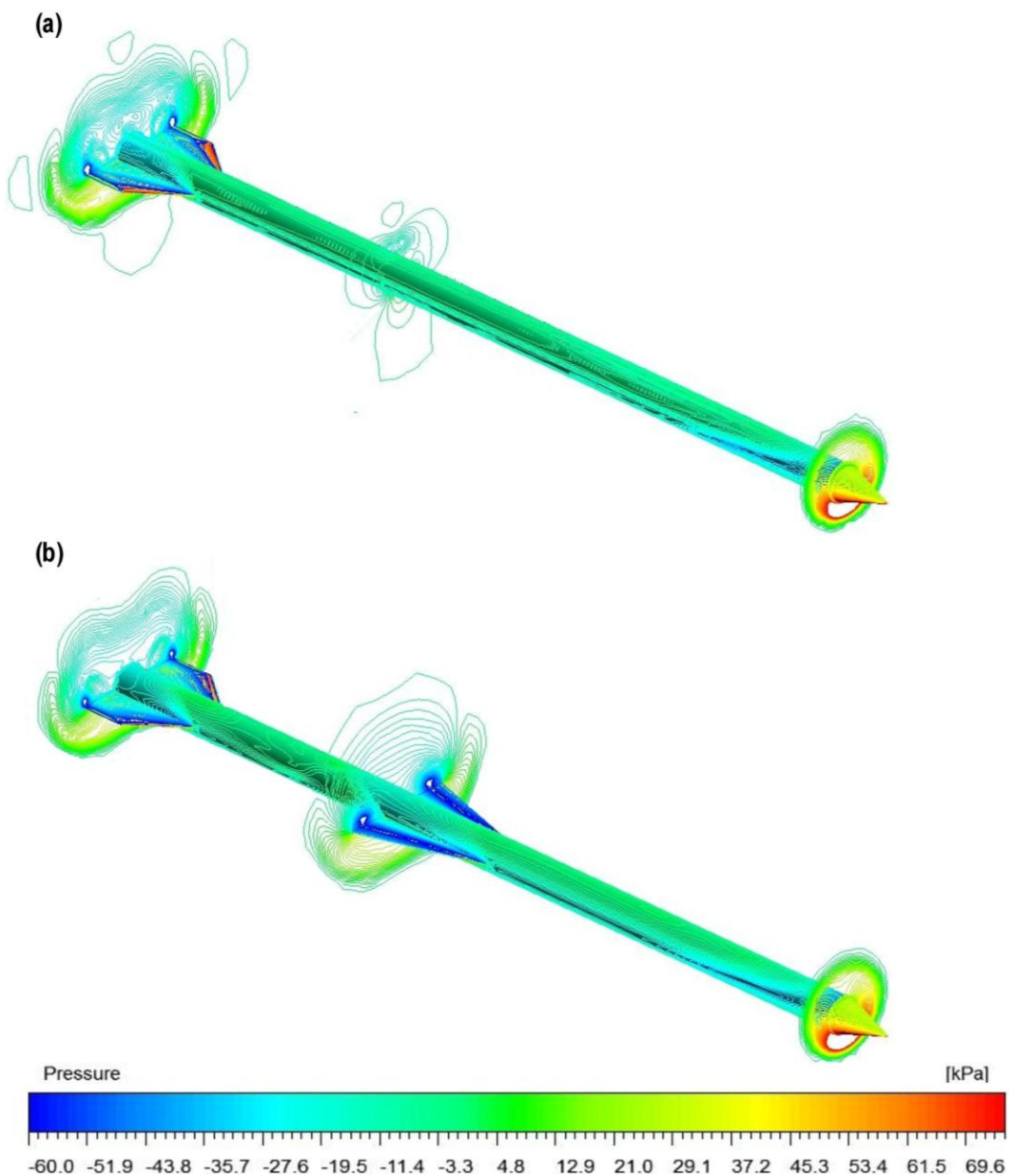


FIGURE 22: Pressure Contour at AOA = 10° of (a) Seamless and (b) Canard Body at  $x = 0.5$  m, 5.5 m and 8.5 m.

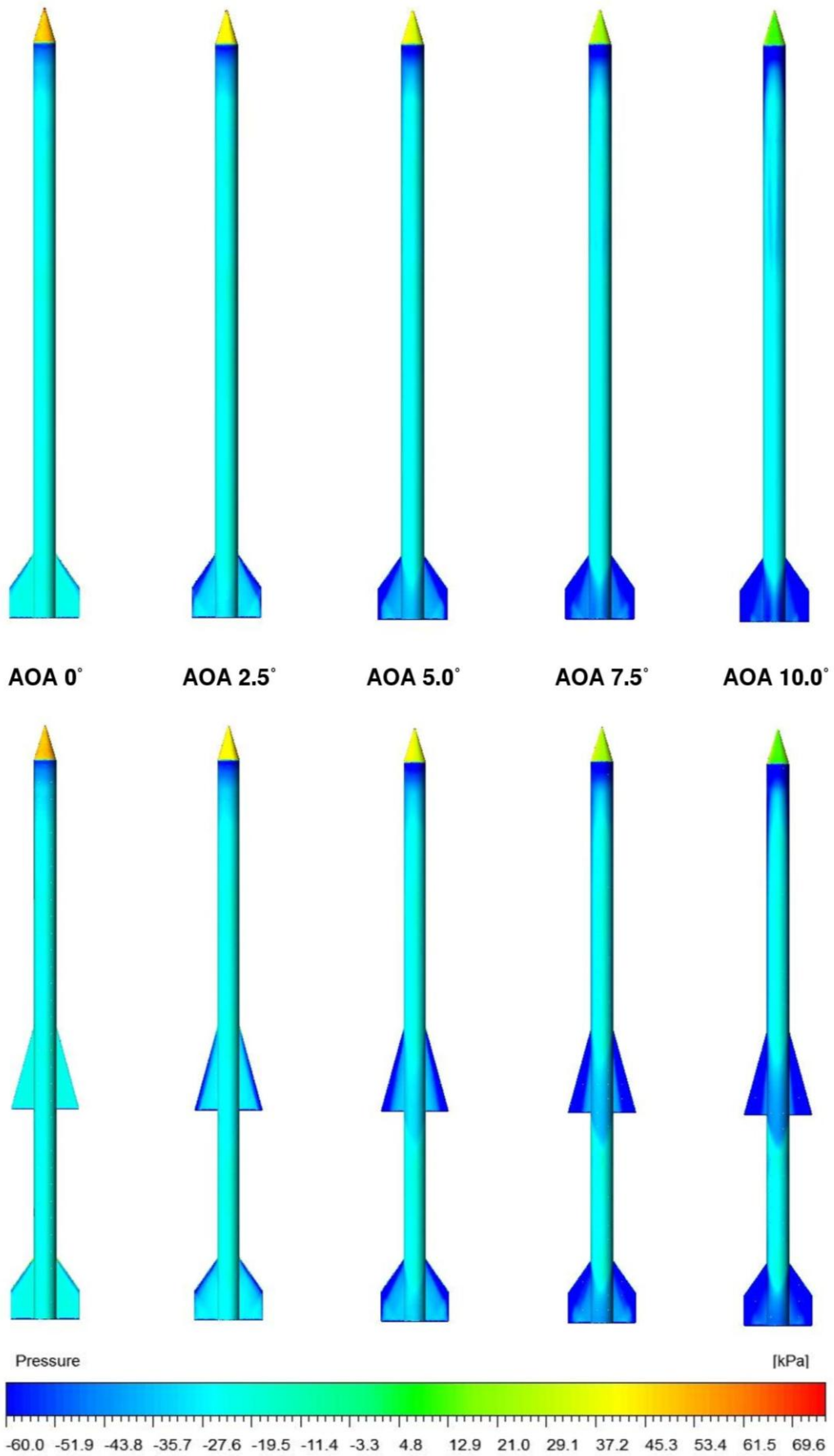


FIGURE 23: Pressure Distribution on the Seamless (Top Row) and Canard (Bottom Row) Body.

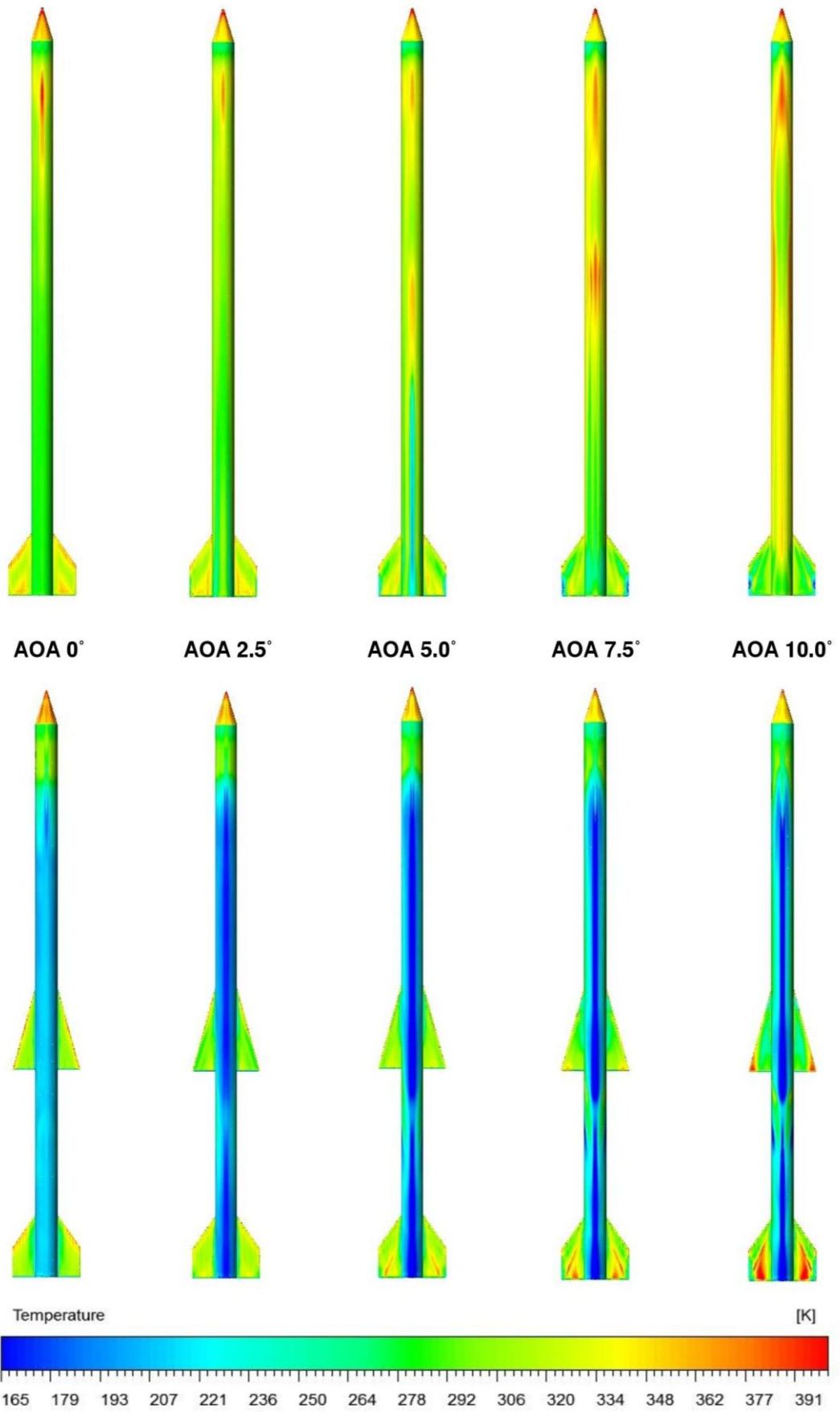


FIGURE 24: Temperature Distribution on Seamless (Top Row) and Canard (Bottom Row) Body.

Meanwhile, Figure 25 presents the vector visualization of the flow field at the rear region of the seamless body. It shows the formation of paired vortices in the wake region, indicated in cyan-blue color vectors.

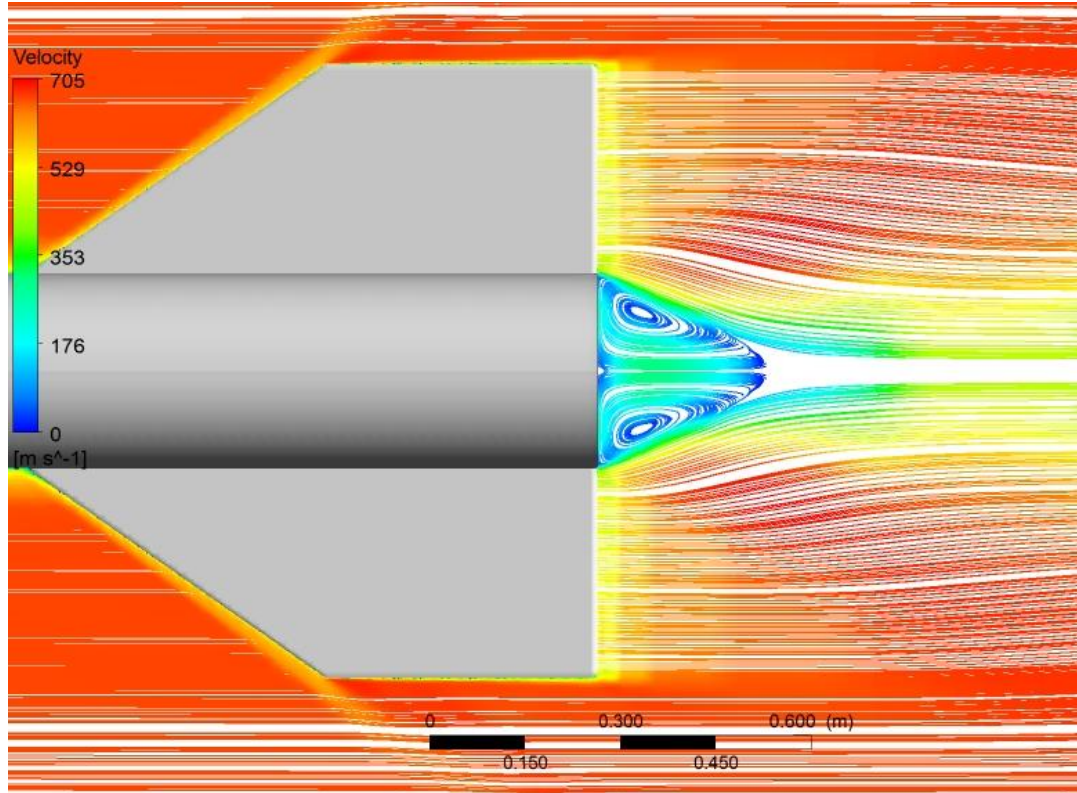


FIGURE 25: Flow Recirculation at Wake Region (Cyan-Blue Color Region) of Seamless Body.

By using streamline visualization in Figure 25, the wake turbulence at the rear part of the seamless body can also be visualized to show the motion of the air at that particular region. A similar phenomenon can also be observed in canard body. It commonly happens when a body with cross-sectional area travels through a fluid medium, such as air. From there, it shows that the motion of the flying bodies through the air induces a recirculating flow at its rear region at low pressure value.

In addition, the vortices formations of the flying bodies are also investigated via streamline visualization, starting from angle of attack of  $2.5^\circ$ . 2 locations,  $x_1 = 5.5$  m and  $x_2 = 8.5$  m of both seamless and canard body are sectioned in the z-y plane and have their streamline visualized. The location  $x_1 = 5.5$  m is supposedly the trailing edge of the canard, which exists only in canard body while location  $x_2 = 8.5$  m is located at the trailing edge of the tail-fin. The comparison of vortices behavior between seamless and canard is as shown in Figure 26 and 27.

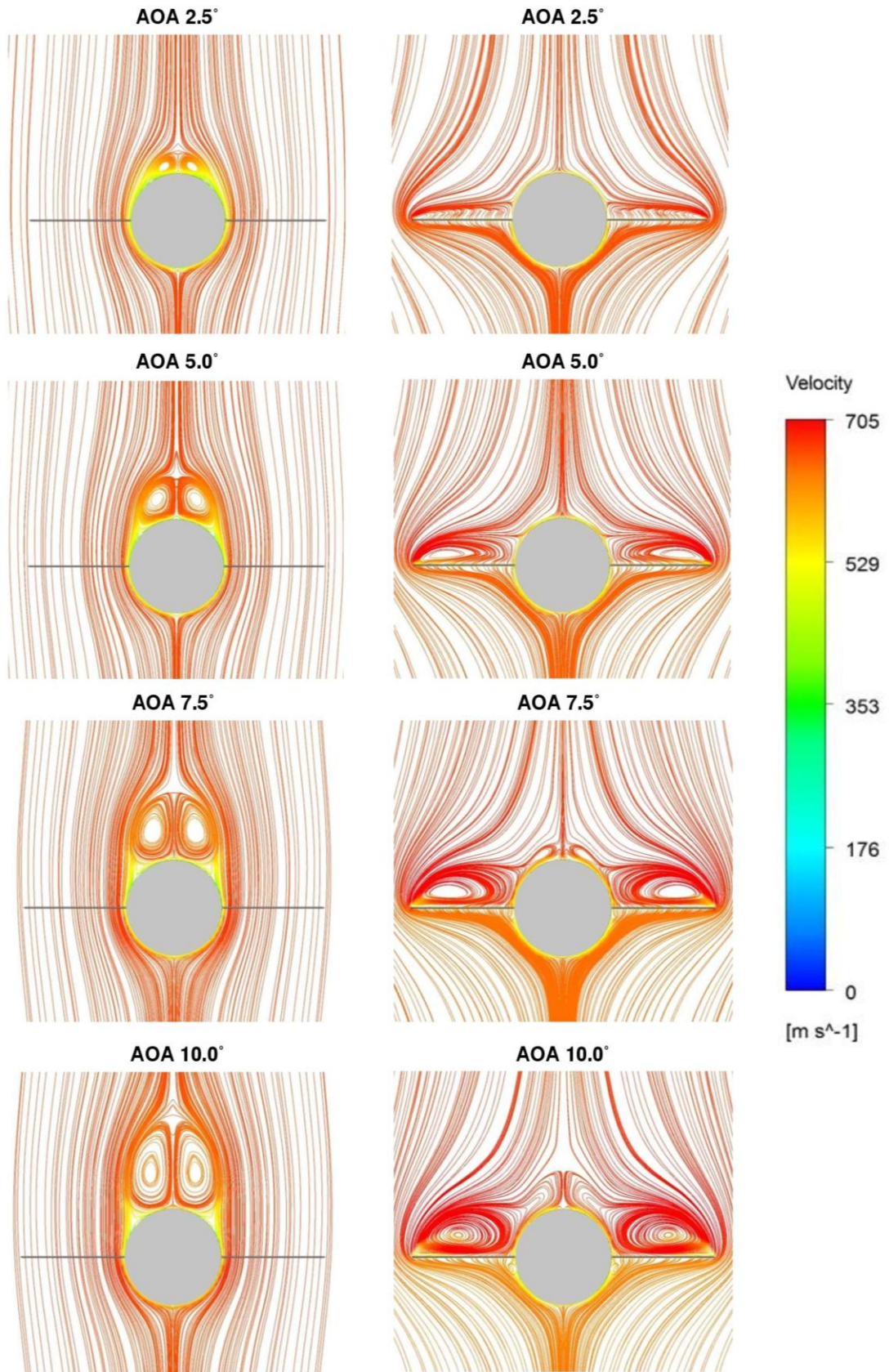


FIGURE 26: Vortices Formation of (Left) Seamless and (Right) Canard Body at  $x = 5.5$  m at Multiple AOAs.



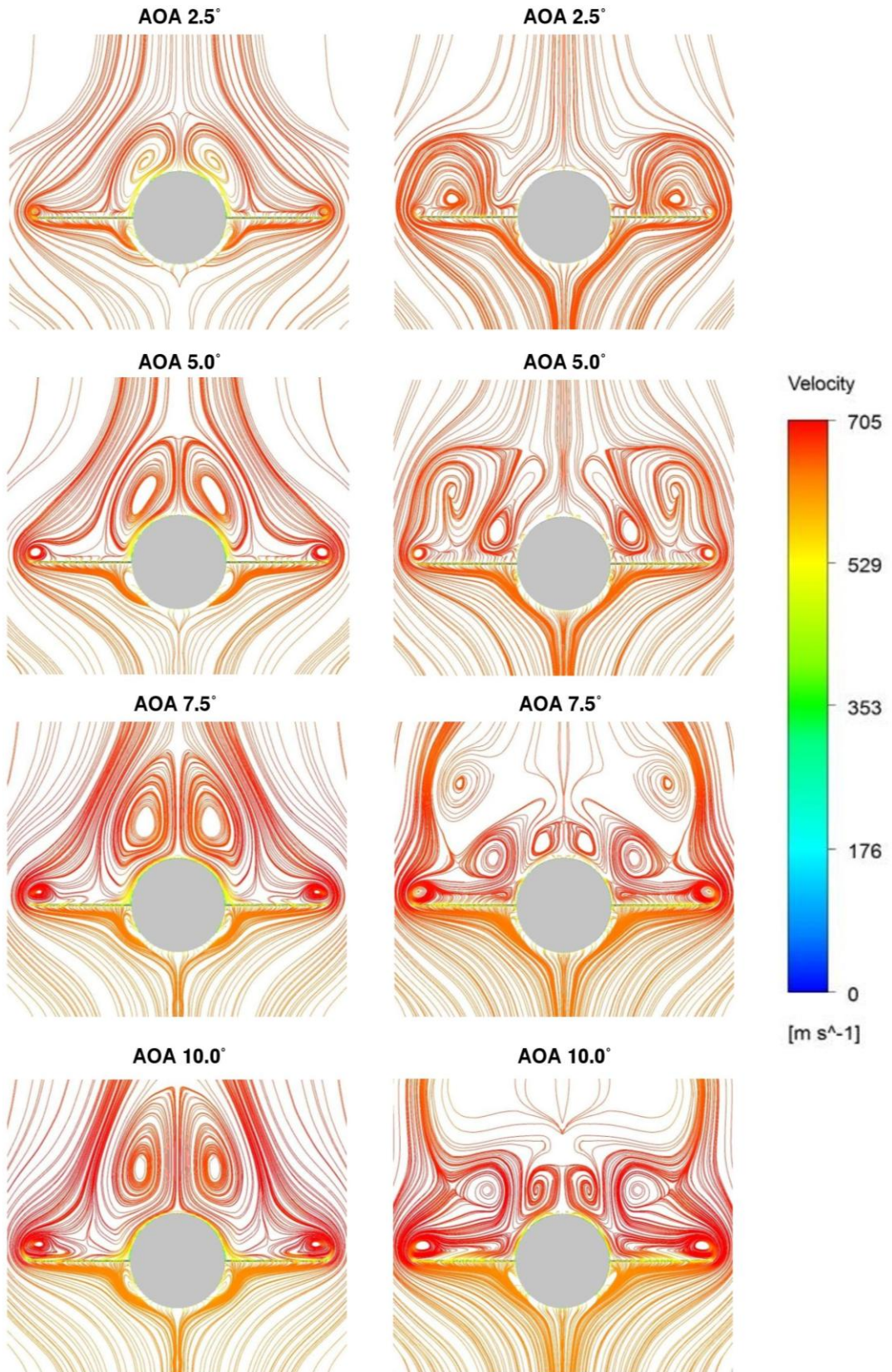


FIGURE 27: Vortices Formation of (Left) Seamless and (Right) Canard Body at  $x = 8.5$  m at Multiple AOAs.

Based on Figure 26, a pair of vortices forms  $x_1 = 5.5$  m above the main body of seamless body and its size grows when the AOA value increases. Moreover, the rotational axis of the vortices also gradually shifts upwards relative to the main body. Conversely, wing tip vortices form at that same location in canard body due to the presence of canard, yielding a rather complicated vortices structure. Similar to the seamless body, the wing tip vortices grow larger in size relative to the angle of attack. In particular, an additional pair of secondary vortices is also observed to be developing on top of its main body, starting from AOA  $7.5^\circ$  onwards.

Likewise, Figure 27 shows the vortices behavior at  $x_2 = 8.5$  m of both seamless and canard body. In seamless body, as the location is at the end of the body, a relatively well developed pair of vortices is formed above the main body and it is accompanied by a pair of small wing tip vortices at the wing tip of the tail-fin. Corresponding to the previous location, the vortices grow larger in size relative to the AOA value increment. However, the vortices behavior at the trailing edge of tail-fin of canard body is complicated and in a disorder manner. Two additional pairs of developing vortices are observed around the upper-half of the main-body apart from the wing tip vortices. At  $7.5^\circ$ , an extra pair of vortices is also observed further above its main body and such phenomenon does not happen at the other AOA values. The complexity of the vortices in canard body's tail-fin is primarily contributed by the flow downwash from the canard, where the canard vortices could propagate downstream and promote the development of vortices at the tail-fin area. This also explains the possibility of lift lost at the tail-fin due to high vorticity intensity in the canard body.

## CHAPTER 5

### CONCLUSION AND RECOMMENDATION

#### 5.1 CONCLUSION

CFD and DATCOM simulations have been conducted on seamless and canard body as a comparison to investigate the effect of canard configuration on a flying body. By analyzing the results, several conclusions can be made as follow.

- CFD and DATCOM results for both seamless and canard body show relatively good agreement in terms of  $C_A$  and  $C_D$ . DATCOM over-predicted the value of  $C_L$ ,  $C_M$  and  $C_N$ . A significant low pressure region forms at the canard when angle of attack is applied. With the presence of canard, canard body yields a higher coefficient than seamless body by a range of 20% to 54% in all aerodynamic forces and moment investigated. The  $L/D$  ratio also improves by approximately 20% in the canard configuration.
- Contour visualization of the flow domain reveals the typical aerodynamic flow field where oblique shock waves form at the nose, canard and tail-fin and their angles change upon the increment of angle of attack. The downwash from canard significantly affect the air properties at the downstream in terms of surface pressure and temperature distribution and vortices behavior at the tail-fin. High temperature accumulates at the wing root of the tail-fin in canard body, which is contributed by the downwash effect. Vortices develop at a slower pace in canard body due to the downwash effect.

#### 5.2 RECOMMENDATION

The aerodynamic characteristics of the flying body studied in this research can be further improved to achieve higher lift and lower induced drag. The findings show that tail-fin of the flying body is having high vorticity intensity, thereby leading to lift lost. The vortices could also be hazardous to other flying bodies when they

encounter the leftover air stream with high vorticity. Therefore, the following improvements can be made on the design of the present seamless and canard body.

- Depending on its application, a blended winglet can be added at the tip of the canard and tail-fin to diffuse the shedding wing-tip vortices and minimizing induced drag.
- Increase the aspect ratio of the canard or tail-fin, depending on the intensity of maneuverability to be achieved, to increase the lift-to drag ratio of the flying body.

In order to further improve the present research, several recommendations which could be used as an extension of this research are proposed as follow.

- Attempt DATCOM simulation using the newer software specially-designed for projectile-shape body simulation, such as MISSILE DATCOM.
- Conduct CFD simulation of the canard body with a longer canard wingspan to investigate if the downwash effect is significant at the area near the tail-fin.
- Simulate seamless and canard body with 4 tail-fins and 4 canards via CFD to compare their aerodynamic behavior with the cases where there are 2 tail-fins and 2 canards only. Deflection angle can also be considered in the simulation.
- Conduct experimental work, such as wind tunnel testing, on the flying body in a high speed wing tunnel and compare the experimental results with the CFD and DATCOM results obtained in the present research.

## REFERENCES

- [1] J. D. Anderson, *Fundamentals of Aerodynamics: Fifth Edition*. New York, NY, 10020: McGraw-Hill, 2011.
- [2] J. D. Anderson, *Modern Compressible Flow With Historical Perspective: Third Edition*. New York, NY, 10020: McGraw-Hill, 2003.
- [3] T. A. Ward, *Aerospace propulsion systems*: John Wiley & Sons, 2010.
- [4] D. A. Frostbutter, B. E. McGrath, and R. P. Rog r, "Application of Computational Fluid Dynamics in Missile Engineering," *Johns Hopkins APL Technical Digest* vol. 22, pp. 289-301, 2001.
- [5] J. D. Anderson, *Computational Fluid Dynamics- The Basics With Applications*. New York: McGraw-Hill, 1995.
- [6] H. H. Al-Kayiem, A. K. Hussein, J. M. Jaleel, and S. H. Hussain, "Numerical Computation of 3-dimensional Supersonic Flow Field over Seamless Missiles," *Indian Journal of Science and Technology*, vol. 7, pp. 1563-1572, 2014.
- [7] E. T. Kim, K. J. Seong, and Y. C. Kim, "A Study on Parameter Estimation for General Aviation Canard Aircraft," *International Journal of Aeronautical and Space Sciences*, vol. 16, pp. 425-436, 2015.
- [8] H. C. Wee, "Aerodynamic Analysis of a Canard Missile Configuration using ANSYS-CFX," Master's Degree Master's Degree Dissertation, Defense Technical Information Center, Naval Postgraduate School, Monterey, California, 2011.
- [9] W.-d. Zhang, Y.-b. Wang, and Y. Liu, "Aerodynamic study of theater ballistic missile target," *Aerospace Science and Technology*, vol. 24, pp. 221-225, 2013.
- [10] H. Tomi, T. Tuomas, and P. Antti, "CFD Simulations and Wind Tunnel Experiments of a Generic Split-Canard Air-to-Air Missile at High Angles of Attack in Turbulent Subsonic Flow," in *AIAA Atmospheric Flight Mechanics Conference*, ed: American Institute of Aeronautics and Astronautics, 2011.
- [11] A. Ridluan, "CFD Investigation of Compressible Low Angles of Attack Flow over the Missile," *Journal of Physical Science and Application*, vol. 4, pp. 339-347, 2014.
- [12] J. Sahu and K. R. Heavey, "Parallel CFD computations of projectile aerodynamics with a flow control mechanism," *Computers & Fluids*, vol. 88, pp. 678-687, 12/15/2013.
- [13] C.-C. Li, C.-S. Tai, C.-C. Lai, S.-M. Fu, and Y.-C. Tsai, "Study of the Aerodynamic Characteristic and Flight Trajectories in a Tail Fin-stabilized Projectile with Different Shapes," *Procedia Engineering*, vol. 79, pp. 108-113, 2014.
- [14] E. G lay, A. Akg l, J. Isakovi , and S. Mandi , "Computational Fluid Dynamics and Experimental Investigation of Wrap-Around-Fins Missile Rolling Moment," *Scientific Technical Review*, vol. 61, pp. 8-15, 2011.
- [15] G. Zhang, S. Yang, and Y. Xu, "Investigation of Vortex Interaction in Canard-FSW Configurations Based on the Numerical Wind Tunnel Method," *Chinese Journal of Aeronautics*, vol. 23, pp. 312-319, 2010.
- [16] K. Xie, Y. Liu, and J. Xin, "Controlled canard configuration study for a solid rocket motor based unmanned air vehicle," *Journal of Mechanical Science and Technology*, vol. 23, pp. 3271-3280, 2009/12/01, 2009.
- [17] B. Kaleeswaran, K. Kowtham Kumar, and S. Ranjith Kumar, "Computational Fluid Dynamic Analysis of Notched Canard Arrangement in Cruise Missiles at Supersonic Flows.," *International Journal of Engineering Research and Development*, vol. 6, pp. 103-111, 2013.

- [18] S. R. Anand and P. S. Kulkarni, "Aerodynamic Performance of the Canard Wing Configuration- A CFD Study," presented at the 16th Annual CFD Symposium, 2014, Bangalore, 2014.
- [19] R. M. Cummings, H. Yang, and Y. Oh, "Supersonic, turbulent flow computation and drag optimization for axisymmetric afterbodies," *Computers & fluids*, vol. 24, pp. 487-507, 1995.
- [20] S. Shinde, A. R. Paul, and A. Jain, "CFD analysis of viscous flow over delta-rectangular wing," in *Engineering and Systems (SCES), 2013 Students Conference on*, 2013, pp. 1-6.
- [21] P. R. Spalart and S. R. Allmaras, "A One-Equation Turbulence Model For Aerodynamic Flows," *La Recherche Aeronautique*, vol. 1, pp. 5-21, 1994.
- [22] M. A. Sohail, C. Yan, M. Y. Younis, M. Afzal, and Z. Maqbool, "Effects of turbulence modeling on aerodynamic characteristics of a conventional tailed missile configuration," in *Mechanical and Electrical Technology (ICMET), 2010 2nd International Conference on*, 2010, pp. 516-520.
- [23] E. Kwak, N. Lee, S. Lee, and S.-i. Park, "Performance Evaluation of Two-Equation Turbulence Models for 3D Wing-Body Configuration," *International Journal of Aeronautical and Space Sciences*, vol. 13, pp. 307-316, 2012.
- [24] A. Akgül, H. Y. Akargün, B. Atak, and O. Göker, "Numerical investigation of NASA tandem control missile and experimental comparison," *Scientific Technical Review*, vol. 62, pp. 3-9, 2012.
- [25] D. Luo, C. Yan, and X. Wang, "Computational study of supersonic turbulent-separated flows using partially averaged Navier-stokes method," *Acta Astronautica*, vol. 107, pp. 234-246, 2015.
- [26] P. Das and A. De, "Numerical investigation of flow structures around a cylindrical afterbody under supersonic condition," *Aerospace Science and Technology*, vol. 47, pp. 195-209, 2015.
- [27] W. B. Blake and W. J. Gillard, "Prediction of vortex interference on a canard controlled missile," in *Aerospace and Electronics Conference, 1988. NAECON 1988., Proceedings of the IEEE 1988 National*, 1988, pp. 444-451 vol.2.
- [28] M. N. Dahalan, V. C. Su, and M. S. Ammoo, "Development Of A Computer Program For Rocket Aerodynamic Coefficients Estimation," *Jurnal Mekanikal*, vol. 28, pp. 28-43, 2009.
- [29] A. F. Maurice, "Aerodynamic Performance Predictions of a SA-2 Missile Using Missile DATCOM," Naval Postgraduate School, Monterey, California 2009.
- [30] E. J. Abney and M. A. McDaniel, "High angle of attack aerodynamic predictions using missile datcom," *AIAA*, vol. 5086, p. 2005, 2005.
- [31] D. J. Lesieur and O. Quijano, "Studies of Vortex Interference Associated with Missile Configurations," in *52nd Aerospace Sciences Meeting*, 2015, pp. 2015-0213.
- [32] H. E. ÇELİKER, O. AKMAN, G. AKAR, and A. Akgül, "Aerodynamic predictions for HB-1 and HB-2 supersonic and hypersonic test cases and comparison with experiment."
- [33] F. Leopold, F. Jagusinski, and C. Demeautis, "Experimental investigation of shock/vortex interaction for slender canard configurations at supersonic speed," in *Instrumentation in Aerospace Simulation Facilities, 2003. ICIASF '03. 20th International Congress on*, 2003, pp. 247-257.
- [34] M. Kanamori and K. Suzuki, "Shock Wave Detection based on the Theory of Characteristics for CFD Results," presented at the 20th AIAA Computational Fluid Dynamics Conference, Honolulu, Hawaii, 2011.
- [35] A. Akgul, E. Gulay, J. Isakovic, and M. Slobodan, "Aerodynamic Characteristics of the Missiles Movable Wing In The Presence Of The Fixed Wing," presented at the 5th International Scientific Conference On Defensive Technologies, OTEH 2012, Belgrade, Serbia, 2012.

- [36] R. E. M. Nasir, W. Kuntjoro, and W. Wisnoe, "Aerodynamic, Stability and Flying Quality Evaluation on a Small Blended Wing-body Aircraft with Canard Foreplanes," *Procedia Technology*, vol. 15, pp. 783-791, 2014.
- [37] Z. M. Ali, W. Kuntjoro, and W. Wisnoe, "Effect of canard to the aerodynamic characteristics of Blended Wing Body airplane," in *Business, Engineering and Industrial Applications (ISBEIA), 2012 IEEE Symposium on*, 2012, pp. 696-700.
- [38] V. M. L. Lopes and R. MotaGirardi, "Analysis of the aerodynamics characteristics of a wing canard configuration with canard deflection, using panel method," in *proceedings of the 18th International Congress of Mechanical Engineering, OuroPreto, MG*, 2005, pp. 6-11.
- [39] W. Shi, X. Y. Deng, Y. K. Wang, and W. Tian, "Interactions of Asymmetric Vortices Over Chined Forebody/Wing Configuration at High Angles of Attack," *Procedia Engineering*, vol. 67, pp. 317-327, 2013.
- [40] S. Samimi, A. Davari, and M. Soltani, "Canard-Wing Interactions In Subsonic Flow," *Iranian Journal of Science and Technology. Transactions of Mechanical Engineering*, vol. 37, p. 133, 2013.
- [41] M. Giuni and R. B. Green, "Vortex formation on squared and rounded tip," *Aerospace Science and Technology*, vol. 29, pp. 191-199, 2013.
- [42] A. R. Davari, M. R. Soltani, F. Askari, and H. R. Pajuhande, "Effects of wing geometry on wing-body-tail interference in subsonic flow," *Scientia Iranica*, vol. 18, pp. 407-415, 2011.
- [43] R. Babigian and S. Hayashibara, "Computational Study of the Vortex Wake Generated by a Three-Dimensional Wing with Dihedral, Taper, and Sweep," presented at the 27th AIAA Applied Aerodynamics Conference, San Antonio, Texas, 2009.
- [44] A. Bojja and P. Garre, "Analysis on Reducing the Induced Drag Using the Winglet at the Wingtip," *International Journal of Engineering Research & Technology (IJERT)*, vol. 2, pp. 51-53, 2013.
- [45] M. A. Azlin, C. F. M. Taib, S. Kasolang, and F. H. Muhammad, "CFD Analysis of Winglets at Low Subsonic Flow," presented at the Proceedings of the World Congress on Engineering 2011 London, U.K., 2011.
- [46] J. D. Anderson, *Introduction to Flight: Sixth Edition*. New York: McGraw-Hill, 2008.
- [47] E. Furbo, "Evaluation of RANS turbulence models for flow problems with significant impact of boundary layers," Master Degree, Technical-Natural Science, Uppsala Universitet, Sweden, 2010.
- [48] J. C. Kurnia, A. P. Sasmito, S. V. Jangam, and A. S. Mujumdar, "Improved design for heat transfer performance of a novel phase change material (PCM) thermal energy storage (TES)," *Applied Thermal Engineering*, vol. 50, pp. 896-907, 2013.
- [49] J. C. Kurnia, A. P. Sasmito, and A. S. Mujumdar, "Simulation of a novel intermittent ventilation system for underground mines," *Tunnelling and Underground Space Technology*, vol. 42, pp. 206-215, 2014.
- [50] J. Lassaline, "Supersonic Right Circular cone at Zero Angle of Attack," *Ryerson University, AE*, vol. 8121, 2009.
- [51] G. L. Feltham, "Study And Simulation Of Three Dimensional Flows At High Supersonic Speeds For Utias 3-D Euler Code Validation With Specific Emphasis On Compression Lift Applications For Supersonic Transport Aircraft.," Bachelor's Degree, Aerospace Science and Engineering, University of Toronto, 2010.

## APPENDICES A

### 1. Mesh Independency Study- Slender Body

Before the slender body is simulated, a mesh independence study is first conducted to determine the number of elements and their corresponding sizes that will produce a mesh that yields an invariant result with further finer mesh. This is to ensure that the correct size of mesh is used without compromising the accuracy of the CFD results. In Figure 12, the number of element used in the mesh was 870, 503, which was already justified by the mesh independency study. In the following page, Table 8 shows the complete mesh independency study of the slender body.

TABLE 8: Mesh Independency Study Results for Slender Body

No.	Nodes No.	Elem. No.	Min Size (Global) in mm	Face Sizing in mm	Inflation in mm	Drag Coefficient, $C_D$	Change in $C_D$ (%)
1	251399	275880	0.00417	0.005	0.005	<b>0.20178302</b>	<b>N/A</b>
2	344555	384334	0.0035	0.004	0.004	<b>0.20137147</b>	<b>0.2</b>
4	457979	516983	0.003	0.0035	0.0035	<b>0.20139959</b>	<b>0.0693</b>
3	635389	728648	0.0025	0.003	0.003	<b>0.20162807</b>	<b>0.113</b>
5	758082	870503	0.00225	0.00275	0.00275	<b>0.20149883</b>	<b>0.064</b>
6	903218	1039148	0.002	0.0025	0.0025	<b>0.20181297</b>	<b>0.156</b>
7	1178249	1370408	0.00175	0.00225	0.00225	<b>0.20170809</b>	<b>0.052</b>

The variable that is examined in the mesh independency study is the drag coefficient,  $C_D$ . Based on Table 8 the change in  $C_D$  remained low than 0.2% when CFD simulations were ran from medium-coarse to fine mesh. Therefore, the mesh independence is considered to be successfully achieved as a finer mesh does not contribute to a major change to the aerodynamic characteristics. As mentioned earlier, the number of element chosen was 870, 503. The reason that this number of element was chosen is because the justification from the independency study and also to anticipate a better resolution of flow field in a finer mesh.



## 2. Mesh Independency Study- Seamless and Canard Body

After the physics and boundary conditions are validated to be accurate using the slender body, the same flow parameters and conditions are applied first to the seamless body. Before that, a mesh independency study was also made for seamless body as presented in Table 9 and 10.

TABLE 9: Mesh Independency Study for Seamless Body, PART 1

No.	Nodes No.	Elem. No.	Min Size (Global)	Face Sizing (Body)	Face Size (NOSE)	Face Size (LE)
1	76298	65,963	0.02	0.08	0.04	0.038
2	130,592	116,362	0.02	0.05	0.02	0.028
3	182,586	169,622	0.02	0.04	0.01	0.025
4	342,740	313,481	0.02	0.02	0.02	0.01
5	405,445	373,872	0.009	0.018	0.018	0.009
6	514,544	475,029	0.008	0.015	0.015	0.008
7	647,249	601,334	0.007	0.012	0.012	0.0075
8	814,247	757,046	0.007	0.011	0.011	0.0073
9	940,979	874,569	0.007	0.0111	0.011	0.0054
10	1,006,605	938,772	0.007	0.0111	0.011	0.0052
11	1,141,761	1,034,820	0.007	0.011	0.011	0.0053

TABLE 10: Mesh Independency Study for Seamless Body, PART 2.

No.	Nodes No.	Elem. No.	Inflation	$C_D$	Change in Drag (%)
1	76298	65,963	2.5e-002	<b>0.31648547</b>	<b>N/A</b>
2	130,592	116,362	5e-003	<b>0.3521076</b>	<b>11.26</b>
3	182,586	169,622	5e-003	<b>0.34380615</b>	<b>2.36</b>
4	342,740	313,481	5e-003	<b>0.35217011</b>	<b>2.43</b>
5	405,445	373,872	5e-003	<b>0.37378342</b>	<b>6.14</b>
6	514,544	475,029	4.5e-003	<b>0.36760924</b>	<b>1.65</b>
7	647,249	601,334	4.2e-003	<b>0.37958491</b>	<b>3.26</b>
8	814,247	757,046	4e-003	<b>0.37608141</b>	<b>0.923</b>
9	940,979	874,569	4e-003	<b>0.3753361</b>	<b>0.198</b>
10	1,006,605	938,772	4e-003	<b>0.37862582</b>	<b>0.876</b>
11	1,141,761	1,034,820	4e-003	<b>0.37512499</b>	<b>0.925</b>

Based on Table 10, the change in  $C_D$  is of high percentage when coarse mesh is used. When the mesh is gradually refined, the variation of  $C_D$  slowly reduces, but it does fluctuate drastically in between the mesh refinement. This indicates that the mesh independency have not reached yet at that stage. Starting from a number of elements of 757, 046 onwards, the  $C_D$  variation further reduces and reaches less than 1%, then

continue to stay within that range. The mesh independency is thus assumed to be achieved. A number of elements of 874,569 is selected as it is capable of producing accurate result after justified by the independency study and to ensure a good resolution for flow field visualization. Table 11 finalizes the mesh parameters for the seamless body which will be used in the actual CFD simulations for future analysis.

TABLE 11: Finalized Mesh Parameters for Seamless Body

No.	Parameters	Settings
1.	Meshing Method	Cut Cell (To Form Hexagonal-Dominant Structured Mesh with Good Quality)
2.	Global Min Size	0.007 mm
3.	Cylinder's Face Size	0.0111 mm
4.	Nose's Face Size	0.011 mm
5.	Leading Edge's Face Size	0.0054 mm
6.	Number of Inflation Layers	10
7.	Inflation Total Thickness	0.004 mm
8.	Number of Nodes	940,979
9.	Number of Elements	874,569

In addition, Table 12 and 13 show the mesh independency study conducted for canard body via the same methodology as the seamless body.

TABLE 12: Mesh Independency Study for Canard Body, PART 1

No.	Nodes No.	Elem. No.	Min Size (Global)	Face Sizing (Body)	Face Size (NOSE)	Face Size (LE)
1	85,454	74,734	0.02	0.08	0.04	0.038
2	123,923	109,458	0.02	0.05	0.02	0.028
3	165,474	151,177	0.02	0.04	0.01	0.025
4	349,500	320,522	0.02	0.02	0.02	0.01
5	405,070	373,040	0.009	0.018	0.018	0.009
6	583,432	547,217	0.008	0.015	0.015	0.008
7	726,269	684,306	0.007	0.012	0.012	0.0075
8	873,018	825,965	0.007	0.0112	0.008	0.0065
9	995,097	958,556	0.007	0.0112	0.008	0.0062
10	1,029,335	987,112	0.007	0.011	0.008	0.0061
11	1,053,073	1,008,302	0.007	0.0112	0.008	0.0062
12	1,208,767	1,154,245	0.007	0.0105	0.0075	0.0052

TABLE 13: Mesh Independency Study for Canard Body, PART 2.

No.	Nodes No.	Elem. No.	Inflation	$C_D$	Change in Drag (%)
1	85,454	74,734	2.5e-002	<b>0.32086916</b>	N/A
2	123,923	109,458	5e-003	<b>0.36802475</b>	<b>14.70</b>
3	165,474	151,177	5e-003	<b>0.377795</b>	<b>2.66</b>
4	349,500	320,522	5e-003	<b>0.3797388</b>	<b>0.515</b>
5	405,070	373,040	5e-003	<b>0.38953178</b>	<b>2.58</b>
6	583,432	547,217	4.5e-003	<b>0.37904531</b>	<b>2.69</b>
7	726,269	684,306	4.2e-003	<b>0.3926514</b>	<b>3.59</b>
8	873,018	825,965	4e-003	<b>0.39067281</b>	<b>0.504</b>
9	995,097	958,556	4e-003	<b>0.39009574</b>	<b>0.148</b>
10	1,029,335	987,112	5e-003	<b>0.39120129</b>	<b>0.283</b>
11	<b>1,053,073</b>	<b>1,008,302</b>	<b>5e-003</b>	<b>0.39070872</b>	<b>0.126</b>
12	1,208,767	1,154,245	5e-003	<b>0.39260358</b>	<b>0.485</b>

Similar to the seamless body, the change in  $C_D$  of canard body at coarse mesh is of high percentage, as shown in Table 13. The  $C_D$  variation starts to stabilize and reaches less than 1% from an element number of 1,008,302 onwards. Thus, the mesh independency is assumed to be achieved. Table 14 finalizes the mesh parameters for the canard body which will be used in the actual CFD simulations for future analysis.

TABLE 14: Finalized Mesh Parameters for Canard Body

No.	Parameters	Settings
1.	Meshing Method	Cut Cell (To Form Hexagonal-Dominant Structured Mesh with Good Quality)
2.	Global Min Size	0.007 mm
3.	Cylinder's Face Size	0.0112 mm
4.	Nose's Face Size	0.008 mm
5.	Leading Edge's Face Size	0.0062 mm
6.	Number of Inflation Layers	10
7.	Inflation Total Thickness	0.005 mm
8.	Number of Nodes	1,053,073
9.	Number of Elements	1,008,302

On the other hand, Table 15 compiles the boundary conditions assignment for each AOA values cases for the named selection surface 1) Inlet, 2) Outlet and 3) Far Field. Those boundary conditions are applied to both seamless and canard body.

TABLE 15: Boundary Conditions for the Named Selection Surface Inlet, Outlet and Far Field

AOA	Mach No.	x-component	y-component	z-component	P (Pa)	T (K)
0°	2	1	0	0	84643	278.4
2.5°	2	0.999048221	0.043619387	0	84643	278.4
5.0°	2	0.996194698	0.087155742	0	84643	278.4
7.5°	2	0.991444861	0.130526192	0	84643	278.4
10.0°	2	0.984807753	0.173648177	0	84643	278.4

Figure 28 shows the typical scaled residual for CFD Simulation of Seamless Body at Mach 2.0 and AOA 0° while Figure 29 shows the  $C_D$  Plot against Iterations.

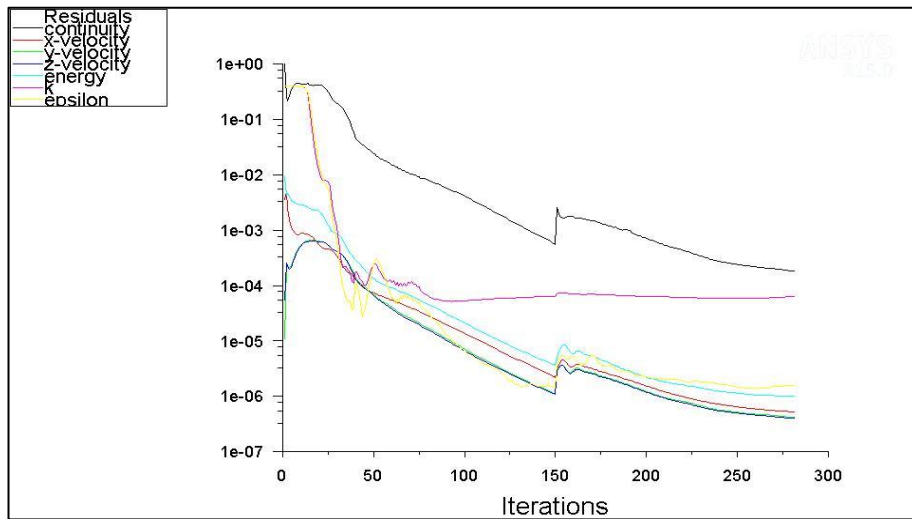


FIGURE 28: Scaled Residual for CFD Simulation of Seamless Body at Mach 2.0 and AOA 0°.

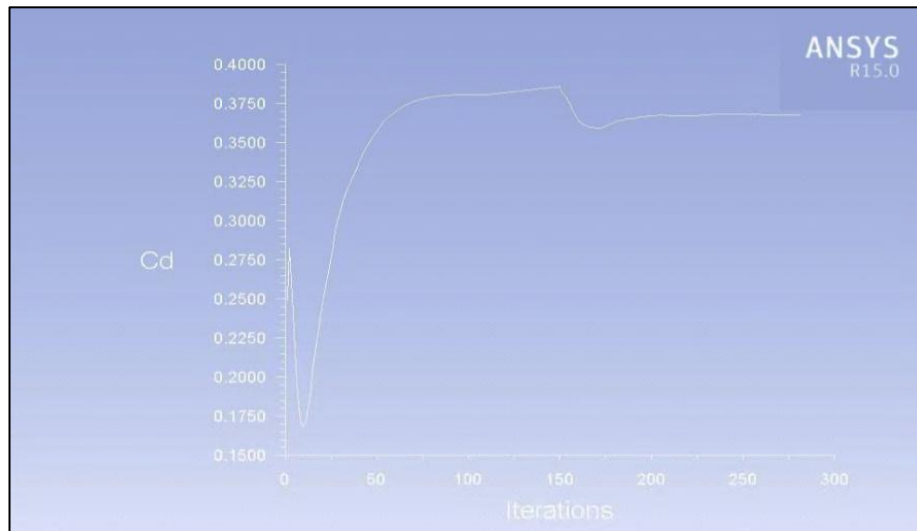


FIGURE 29:  $C_D$  Plot against Iterations of Seamless Body.

### 3. DATCOM Code for Semi-Empirical Simulation

#### a. Seamless Body

DIM M

```
$FLTCON NMACH=1.0, MACH(1)=2.0, RNNUB(1)=3.45E8,  
NALPHA=5.0, ALSCHD(1)=0.0,2.5,5.0,7.5,10.0,  
NALT=1.0, ALT(1)=1500.0,HYPERS=.FALSE.$  
$OPTINS SREF=0.074,CBARR=8.5$  
$SYNTHS XCG=0.0, ZCG=0.0,SCALE=1.0$  
$BODY NX=10.0,BNOSE=2.0, BTAIL=2.0, BLN=0.5, BLA=0.0,  
X(1)=0.0,0.25,0.5,2.1,3.7,  
5.3,6.0,6.9,7.5,8.5,  
S(1)=0.0,0.0184,0.0735,0.0735,0.0735,  
0.0735,0.0735,0.0735,0.0735,0.0735,  
P(1)=0.0,0.4807,0.9613,0.9613,0.9613,  
0.9613,0.9613,0.9613,0.9613,0.9613,  
R(1)=0.0,0.0765,0.153,0.153,0.153,  
0.153,0.153,0.153,0.153,0.153$
```

NACA-W-S-2-0.3763-1.0-0.992

```
$WGPLNF CHSTAT=5.0, SWAFP=0.0,  
TWISTA=0.0,SSPNDD=0.0,DHDADI=0.0,DHDADO=0.0,TYPE=1.0$  
$SYNTHS XW=7.38,ZW=0.0,ALIW=0.0$  
$WGPLNF CHRDTTP=0.42871,  
SSPNE=0.33,SSPN=0.483,CHRDR=1.12,SAVSI=55.0$
```

CASEID SEAMLESS BODY, CASE 1

NEXT CASE

**b. Canard Body**

DIM M

\$FLTCON NMACH=1.0, MACH(1)=2.0,  
NALPHA=5.0, ALSCHD(1)=0.0,2.5,5.0,7.5,10.0,  
NALT=1.0, ALT(1)=1500.0,HYPERS=.FALSE.\$  
\$OPTINS SREF=0.074,CBARR=8.5\$  
\$SYNTHS XCG=0.0, ZCG=0.0,SCALE=1.0\$  
\$BODY NX=10.0,BNOSE=2.0, BTAIL=2.0, BLN=0.5, BLA=0.0,  
X(1)=0.0,0.25,0.5,2.1,3.7,  
5.3,6.0,6.9,7.5,8.5,  
S(1)=0.0,0.019,0.074,0.074,0.074,  
0.074,0.074,0.074,0.074,0.074,  
P(1)=0.0,0.48,0.96,0.96,0.96,  
0.96,0.96,0.96,0.96,0.96,  
R(1)=0.0,0.077,0.153,0.153,0.153,  
0.153,0.153,0.153,0.153,0.153\$

NACA-W-S-2-0.3763-1.0-0.992

NACA-H-S-2-0.3763-1.0-0.992

\$WGPLNF CHSTAT=4.0, SWAFP=0.0,  
TWISTA=0.0,SSPNDD=0.0,DHDADI=0.0,DHDADO=0.0,TYPE=1.0\$  
\$SYNTHS XW=3.744,ZW=0.0,ALIW=0.0\$  
\$WGPLNF CHRDTTP=0.0,  
SSPNE=0.33,SSPN=0.483,CHRDR=1.7564,SAVSI=15.376\$  
\$SYNTHS XH=7.38,ZH=0.0,ALIH=0.0\$  
\$HTPLNF SSPNE=0.33,SSPN=0.483,CHRDR=1.1185,SAVSI=55.0,  
CHSTAT=0.0,  
CHRDTTP=0.42871,TYPE=1.0\$

CASEID CANARD BODY, CASE 2

NEXT CASE

## 4. Post-Processed DATCOM Results in MATLAB

```

p Window Help
Current Folder: C:\Users\acer\Desktop\Final Year 1st Sem\FYP\Digital DATCOM\datcomexec

Command Window
New to MATLAB? Watch this Video, see Demos, or read Getting Started.

0      *** CREST CRITICAL MACH NUMBER EXCEEDED ***

      CREST CRITICAL MACH = 0.87277

      LOCATION = 0.06111 FRACTION CHORD

      LIFT-CURVE-SLOPE = 0.18894 /DEG.
1      AUTOMATED STABILITY AND CONTROL METHODS PER APRIL 1976 VERSION OF DATCOM
      CHARACTERISTICS AT ANGLE OF ATTACK AND IN SIDESLIP
      WING-BODY CONFIGURATION
      SEAMLESS BODY PLUS WING, CASE 1

----- FLIGHT CONDITIONS -----
MACH  ALTITUDE  VELOCITY  PRESSURE  TEMPERATURE  REYNOLDS  REF.  REFERENCE DIM
NUMBER  M          M/SEC    N/ M**2   DEG K       NUMBER    AREA   LONG.  LAT.
0 2.000  1500.00   668.90   8.4560E+04 278.402    3.4500E+08 0.074  8.500  0.966
0
0 ALPHA  CD      CL      CM      CN      CA      XCP      CLA      CMA      CYB      CN
0
0      0.0   0.324  0.000  0.0000  0.000  0.324  *****  1.152E-01  -9.650E-02  -3.760E-02  3.808
      2.5   0.336  0.388  -0.3230  0.403  0.319  -0.802  1.982E-01
      5.0   0.393  0.991  -0.8018  1.022  0.305  -0.785  2.671E-01
      7.5   0.522  1.724  -1.4211  1.777  0.293  -0.800  3.354E-01
      10.0  0.756  2.668  -2.1851  2.759  0.281  -0.792  4.201E-01
1      THE FOLLOWING IS A LIST OF ALL INPUT CARDS FOR THIS CASE.
0
1 END OF JOB.

fx >>

```

FIGURE 30: DATCOM Simulation Results in MATLAB for Seamless Body.

```

dow Help
Current Folder: C:\Users\acer\Desktop\Final Year 1st Sem\FYP\Digital DATCOM\datcomexec

Command Window
New to MATLAB? Watch this Video, see Demos, or read Getting Started.

      CREST CRITICAL MACH = 0.87277

      LOCATION = 0.06111 FRACTION CHORD

      LIFT-CURVE-SLOPE = 0.18894 /DEG.
1      AUTOMATED STABILITY AND CONTROL METHODS PER APRIL 1976 VERSION OF DATCOM
      CHARACTERISTICS AT ANGLE OF ATTACK AND IN SIDESLIP
      WING-BODY-HORIZONTAL TAIL CONFIGURATION
      CANARD BODY, CASE 2

----- FLIGHT CONDITIONS -----
MACH  ALTITUDE  VELOCITY  PRESSURE  TEMPERATURE  REYNOLDS  REF.  REFERENCE DIM
NUMBER  M          M/SEC    N/ M**2   DEG K       NUMBER    AREA   LONG.  LAT.
0 2.000  1500.00   668.90   8.4560E+04 278.402    4.0449E+07 0.074  8.500  0.966
0
0 ALPHA  CD      CL      CM      CN      CA      XCP      CLA      CMA      CYB      CN
0
0      0.0   0.348  0.000  0.0000  0.000  0.348  *****  2.669E-01  -2.053E-01  -3.760E-02  3.173
      2.5   0.373  0.725  -0.5363  0.740  0.341  -0.725  2.769E-01  -2.145E-01
      5.0   0.469  1.571  -1.0738  1.606  0.331  -0.669  2.763E-01  -2.148E-01
      7.5   0.671  2.413  -1.6201  2.480  0.350  -0.653  2.758E-01  -2.160E-01
      10.0  1.005  3.420  -2.1807  3.542  0.396  -0.616  2.752E-01  -2.181E-01
NOTE - CANARD CONFIGURATION EFFECTIVE EPSOLN AND D(EPSOLN)/D(ALPHA) ARE AVAILABLE AS PARTIAL OUTPUT AND IN I
1      THE FOLLOWING IS A LIST OF ALL INPUT CARDS FOR THIS CASE.
0
1 END OF JOB.

fx >>

```

FIGURE 31: DATCOM Simulation Results in MATLAB for Canard Body.